

# Assembly of Magneto-Fluorescent Supernanoparticles for use as Drug Delivery Vehicles

---

Author:

Aske Bredow Bojesen

Supervisors:

Leonid Gurevich

Peter Fojan



**AALBORG UNIVERSITY**

STUDENT REPORT

MASTER PROJECT

NANOBIOTECHNOLOGY

AALBORG UNIVERSITY

JUNE 2020





**AALBORG UNIVERSITY**  
STUDENT REPORT

**Department of Materials and  
Production**

Aalborg University

Skjernvej 4A

9220 Aalborg Øst

<http://www.nano.aau.dk>

**Title:**

Assembly of Magneto-Fluorescent Supernano-  
particles For Use As Drug Delivery Vehicles

**Project:**

Master project

**Project Period:**

September 2019 - June 2020

**Participants:**

Aske Bredow Bojesen

**Supervisors:**

Leonid Gurevich

Peter Fojan

**Total Page Number: 70**

**Finished: 3rd June 2020**

**Abstract:**

In this report the assembly of magneto-fluorescent supernanoparticles intended for use as drug delivery vehicles is detailed. Iron oxide nanoparticles were synthesised using two different synthesis methods, a co-precipitation method and a thermal decomposition method. CdSe quantum dots were synthesized using two variations of thermal decomposition synthesis, and the formation of a CdS shell around the quantum dots was performed to improve fluorescence. Finally supernanoparticles were assembled using the synthesised iron oxide nanoparticles and quantum dots with CdS shell, and showed clear magneto-fluorescent behaviour.

*The content of this report is freely available, but publication (with source reference) may only take place in agreement with the authors.*



---

# Preface

---

This report is written by a master student in the Fall and Spring semester of 2019-2020 from the 1<sup>st</sup> of September to the 3<sup>rd</sup> of June 2020. The report was developed as a master project of the study program of Nanobiotechnology, School of Engineering and Science at Aalborg University. The report will start with an introduction and then cover general information about the blood brain barrier, drug delivery, iron oxide nanoparticle synthesis and quantum dot synthesis. Thereafter a description of the experimental methods used in this project, followed by obtained results and discussion upon these will be presented. Lastly, a conclusion and proposal of further experimentation is given.

Abbreviations are used throughout this report. References are written using numbers, presenting a number in brackets relating to a specific source in the bibliography. These sources list the name and surname of the authors, title, journal with volume, issue and page numbers or publisher and year of publication listed in this order. In cases of three or more authors, the first author's name is written followed by *et al.* Figures without references are created by the authors of this report.

---

Aske Bredow Bojesen



---

# List of Abbreviations

---

<b>NTA</b>	Nanoparticle Tracking Analysis
<b>SEM</b>	Scanning electron microscope
<b>STEM</b>	Scanning transmission electron microscopy
<b>EDS</b>	Energy-dispersive X-ray spectroscopy
<b>DLS</b>	Dynamic light scattering
<b>MQ</b>	Milli-Q
<b>FWHM</b>	Full width at half maximum
<b>PVP</b>	Polyvinylpyrrolidone



---

# Contents

---

<b>1</b>	<b>Introduction</b>	<b>9</b>
<b>2</b>	<b>The Blood-Brain Barrier</b>	<b>11</b>
2.1	Blood-neural barriers . . . . .	11
2.2	The Neurovascular Unit . . . . .	12
2.3	Tight Junctions . . . . .	13
2.4	In Vitro Blood-Brain Barrier Models . . . . .	13
<b>3</b>	<b>Drug Delivery</b>	<b>15</b>
3.1	Drug Delivery Pathways . . . . .	15
3.2	The Transcellular Pathway . . . . .	16
3.3	Nanoparticle Based Drug Delivery . . . . .	16
<b>4</b>	<b>Iron Oxide Nanoparticle Synthesis</b>	<b>19</b>
4.1	Superparamagnetic Iron Oxide Nanoparticles . . . . .	19
4.2	Hydrolysis Based Synthesis . . . . .	20
4.3	Thermal decomposition Based Synthesis . . . . .	20
4.4	Surface Functionalization . . . . .	20
<b>5</b>	<b>Quantum Dot Synthesis</b>	<b>23</b>
5.1	Thermal decomposition Based Synthesis of Quantum Dots . . . . .	23
5.2	Spectroscopy of Quantum Dots . . . . .	25
5.3	Shell Formation . . . . .	26
<b>6</b>	<b>Materials and Methods</b>	<b>27</b>
6.1	Co-Precipitation Synthesis of Iron oxide Nanoparticles . . . . .	27
6.1.1	Materials . . . . .	27
6.1.2	Method . . . . .	27
6.2	Thermal decomposition synthesis of Iron oxide nanoparticles . . . . .	28
6.2.1	Materials . . . . .	28
6.2.2	Methods . . . . .	28
6.3	Thermal Decomposition Synthesis of Quantum dots . . . . .	29
6.3.1	Materials . . . . .	29
6.4	CdS Shell Synthesis . . . . .	30

6.4.1	Materials . . . . .	31
6.5	Supernanoparticle Synthesis . . . . .	31
6.5.1	Materials . . . . .	32
6.5.2	Methods . . . . .	32
<b>7</b>	<b>Results</b>	<b>33</b>
7.1	NTA measurements of Iron Oxide Nanoparticles . . . . .	33
7.2	SEM Imaging of Iron Oxide Nanoparticles . . . . .	34
7.3	DLS measurements of Iron Oxide Nanoparticles . . . . .	38
7.4	Absorption Spectroscopy Measurements of Quantum Dots . . . . .	39
7.5	Fluorescence Spectroscopy Measurements . . . . .	43
7.6	Fluorescence Microscopy of Super Nanoparticles . . . . .	49
7.7	NTA measurements of Super Nanoparticles . . . . .	51
7.8	STEM Imaging and EDS Spectroscopy of Super Nanoparticles . . . . .	53
<b>8</b>	<b>Discussion</b>	<b>59</b>
8.1	Iron Oxide Nanoparticles . . . . .	59
8.1.1	Co-Precipitation Synthesis of Iron Oxide Nanoparticles . . . . .	59
8.1.2	Silica Coating of Iron Oxide Nanoparticles . . . . .	59
8.1.3	Thermal Decomposition Synthesis of Iron Oxide Nanoparticles . . . . .	60
8.2	Quantum Dots . . . . .	60
8.2.1	Method 1 . . . . .	60
8.2.2	Method 2 . . . . .	61
8.2.3	CdS Shell Synthesis . . . . .	62
8.3	Supernanoparticles . . . . .	62
<b>9</b>	<b>Conclusion</b>	<b>65</b>
<b>10</b>	<b>Further Experimentation</b>	<b>67</b>
	<b>Bibliography</b>	<b>69</b>

---

# 1. Introduction

---

Brain disorders, such as Alzheimer's, Parkinson's and brain cancer, prove serious, yet difficult to treat, health problems.[1] This is in part due to the blood brain barrier, separating most therapeutic agents, commonly delivered through the blood, from the affected tissue. A potential solution to this problem is the transferrin receptor pathway, that bridges the blood brain barrier. However, strong binding to the receptor can prevent successful drug delivery of vehicles utilizing this pathway.[2] A possible remedy to this is the use of magnetic particles, using the guidance of an external magnetic field to guide drug delivery vehicles across the barrier.

The topic of this report is the assembly of magneto-fluorescent supernanoparticles from iron oxide nanoparticles and quantum dots with CdS shell. The purpose of these supernanoparticles is the exploration of blood brain barrier penetration with magnetic guidance, using an in vitro model of the blood brain barrier. The fluorescent properties are key to evaluate penetration of the barrier. CdSe quantum dots coated with CdS show excellent fluorescent properties, and in combination with iron oxide nanoparticles allow for the assembly of nanoparticles with excellent magnetic and fluorescent properties.[3]

Two different iron oxide nanoparticle synthesis methods are explored as well as two different quantum dot syntheses. Silica coating is attempted on the iron oxide synthesis along with CdS shell synthesis on particles from both quantum dot syntheses. Finally supernanoparticle assembly is performed.



---

## 2. The Blood-Brain Barrier

---

Brain disorders such as Alzheimer's, Parkinson's, multiple sclerosis, depression, epilepsy and brain tumors represents one the most serious health burdens of modern society, with hundreds of thousands of people getting diagnosed with these diseases every year. Despite this, brain disorders remain as some of the most prevalent and notably untreatable diseases, with few drugs being efficacious at treating them.[1][4] One of the major hurdles for designing drugs to treat these diseases lies outside the pathology of the diseases themselves. The central nervous system is specifically partitioned from the blood of the vascular system by a number of barriers the foremost of which is the blood-brain barrier. As such, any drug designed for the treatment of brain disorders might be found ineffective due to the drug being unable to reach the affected tissue.[1]

The blood-brain barrier, despite being an obstacle in diagnosis and treatment of brain disorders, is vital to the healthy functioning of the central nervous system, with many brain disorders being linked to the deterioration of the barrier. The brain is reliant on the blood-brain barrier to maintain a very careful homeostasis and ion-balance. The central nervous system also differs from the rest of the body in being sensitive towards many substances and metabolites present in the body that anywhere else are entirely non-toxic, as such requiring careful selection of substances crossing the barrier to maintain a regulated micro-environment. This results in approximately 98% of all small molecules, depending on physico-chemical properties, and virtually all larger molecules, including therapeutic agents such as peptides, proteins, anti-sense agents and other therapeutic macromolecules, to be excluded from the central nervous system.[1]

### 2.1 Blood-neural barriers

The separation between blood and the central nervous system is specialized wherever neural tissue connects to the vascular system, and can be separated into at least five distinct blood-neural barriers. These consist of a organized network of endothelial structures and include the blood-CSF barrier which bridges the cerebrospinal fluid, the arachnoid barrier which bridges the arachnoid, the blood-retinal barrier which bridges the retina, the blood-spinal cord barrier which bridges the spinal cord, and most notably the blood-brain barrier. The blood-brain barrier connects and supplies the brain through an extensive

network of microvessels, the percentage of brain volume of which is estimated for perfused capillaries at 3-4% and for small arterioles and venules at 4-6%. The mean length of these microvessels is 40  $\mu\text{m}$  and for the whole brain totals approximately 650km with a surface area available for transport of about 20  $\text{m}^2$ . [5]

## 2.2 The Neurovascular Unit

The major endothelial structures that make up the blood-brain barrier are brain capillary endothelial cells, pericytes, astrocytes and the basal membrane all of which closely interact with neurons. The organization of these structures form the neurovascular unit, see figure 2.1. Endothelial cells line the inside of the brain capillaries form the bulk of the barrier. Contrary to peripheral capillaries that have fenestrations of up to 50 nm between endothelial cells, the endothelial cells of the brain capillaries form a tight network of cells bridged by tight junction protein structures. [5] Pericytes are vascular smooth muscle cells and contract and relax to regulate microvessel blood flow. Pericytes help regulate endothelial cells and cover about 20% of the abluminal endothelial surface. [5] Astrocytes play an important role in development and maintenance of the neurovascular unit. Astrocyte endfeet cover the brain capillaries and connect to neighboring neurons. In vitro cultures of endothelial cells co-cultured with astrocytes show improved functionality of the blood-brain barrier. [5] The basal membrane is a 30-40 nm thick membrane supporting the endothelial cells and pericytes. The basal membrane also seems to be involved regulation through matrix proteins. [5] While neurons are not directly structurally involved in the blood-brain barrier, the microvascular system of the brain must be responsive to the requirements of neighboring neural tissue and as such prove an important role in the regulation of the blood-brain barrier. [5]

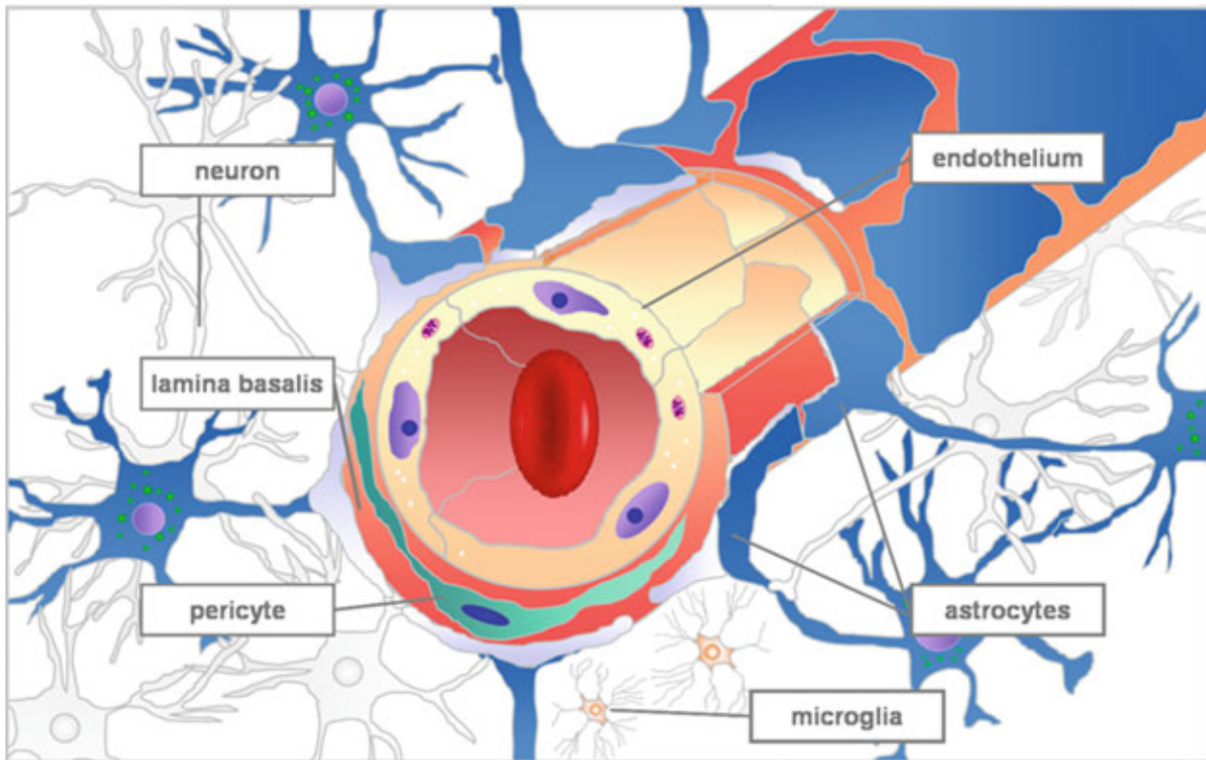


**Figure 2.1:** Cross section of the neurovascular unit, comprised of endothelial cells, astrocytes, pericytes, the basal membrane and neurons.[5]

## 2.3 Tight Junctions

The tight junction of the endothelial cells are critical to maintaining an exclusionary barrier. The tightly packed endothelial cells are joined in three layers of protein structures. The top, blood side, part of the intercellular junction consists of occludins, claudins and junctional adhesion proteins, joined by homeophilic interactions and form the impermeable part of the junction, allowing only molecules of hydrodynamic size 11 Å or smaller through. This allows only small polar molecules such as water, glycerol and urea to permeate across the junction. Below the top layer of the junction is the adherens junction, and is responsible for the tight adherence of the endothelial cells. On the abluminal face of the junction is bridged by the desmosomes. All the intercellular junction proteins are involved in cross talk between the endothelial cells through their cytoskeleton.[1]

## 2.4 In Vitro Blood-Brain Barrier Models

An effective way to evaluate blood-brain barrier behavior and screen drug delivery solutions is through the use of in vitro blood-brain barrier models. One such model is brain endothelial cell monolayer cultures using either primary or immortalized cells. These are

cultured on microporous membrane filters, either as isolated cultures, or as co-cultures with other components of the neurovascular unit, particularly astrocytes and pericytes, to closer model the behavior of brain microvessels. To evaluate model viability the trans-endothelial electrical resistance is commonly measured. A tight layer of endothelial cells along with well developed tight junctions severely reduce movement of charge carriers across the culture. As such the trans-endothelial electrical resistance is an important measure of the successful development as well as macroscopic tears of the barrier. Microfluidic chip based models have also been developed for endothelial cell cultures, using significantly lower cell numbers, sample sizes, and measuring trans-endothelial electrical resistance continuously over development. Generally, in vitro blood-brain barrier models are less expensive and better suitable for high throughput approaches compared to in vivo models.[2]

---

## 3. Drug Delivery

---

Drug delivery to the central nervous system is complicated by the separation of blood from the nervous system through several barriers, most notably the blood-brain barrier.

### 3.1 Drug Delivery Pathways

Several different delivery strategies to penetrate or circumvent the blood brain barrier exist. A simpler method is using olfactory pathways, though is complicated by inflammation of mucosal lining and low pH environments. A more direct method to circumvent the blood-brain barrier is through the use of intraventricular infusion, where therapeutic agents are directly injected into the brain. This method, despite being invasive, lacks efficiency, provides treatment only to tissue near the injection site and is still limited by the blood-CSF barrier. While the blood-brain barrier is highly exclusionary for most therapeutic substances, other barriers of the central nervous system offer less resistance toward delivery. Capillaries of circumventricular organs of the brain allow many drugs, that are otherwise excluded by the blood-brain barrier, passage over the blood-cerebrospinal fluid barrier. However, diffusion from the cerebrospinal fluid into the brain is a slow and short range delivery vehicle, exacerbated by the quick turnover rate of the cerebrospinal fluid, and as such may allow for drug delivery to only a much more limited amount of tissue.[4]

For delivery of drugs through the blood-brain barrier exist two major pathways: paracellular pathways and transcellular pathways. The intercellular region between endothelial cells are occupied by tight junctions and will prevent all but the smallest molecules passage into the central nervous system. One method to allow for larger therapeutic molecules across this paracellular pathway is by increasing the porosity of these intercellular junctions. This has been done by shrinking the endothelial cells by osmotic pressure, increasing the gaps between cells for several hours. Methods to disrupt the proteins of the tight junctions have also been developed. This strategy however interferes with the vital function of the blood-brain barrier, disrupting homeostasis of the central nervous system and predisposing the brain to the influence of toxic substances and infections.[4][2]

## 3.2 The Transcellular Pathway

Passage across the blood-brain barrier for most cerebral nutrients and other vital compounds is through the transcellular pathway. The endothelial cells of the brain microvessels have a complex network of transport proteins and receptors which tightly regulate passage across the barrier. Passive passage across the blood brain barrier, through diffusion across the endothelial cell membrane, is possible for a specific subset of lipid-soluble molecules with a weight below at least 400 Da. For many molecules passage through the endothelial cell is further inhibited by high concentrations of degrading enzymes and efflux pumps.[4][2] A strategy for improving delivery efficacy of a drug is by altering the physico-chemical properties to allow for diffusion through the membrane through the addition of hydrophobic moieties. The formation of this prodrug is reversed after delivery to the brain tissue. Prodrugs are however still vulnerable to efflux pumps and early conversion to the parent drug through enzymatic action before complete delivery.[4][2] For larger compounds where passive diffusion is impossible, receptor mediated transport represent a possible pathway. Exploiting native receptors on the endothelial cell surface, using either the target ligand or specialized monoclonal antibodies, a wider range of drug payloads can be carried into the brain. Among the receptors for possible use is transferrin and insulin receptors. The transferrin receptor works by binding to the iron carrying holo-transferrin which is released in the endosome intracellular, after which the receptor is recycled to the cell surface. While the transferrin receptor has garnered significant interest for drug delivery, actual brain deposition rate of payloads is low. A reason for this is the trapping of monoclonal antibodies in the endothelial cells, due to high binding affinity with the receptor preventing the successful release.[4][2]

## 3.3 Nanoparticle Based Drug Delivery

Nanoparticle based drug carriers are a promising field of research for drug delivery, allowing encapsulation and delivery of large range of compounds, modification of biodistribution, metabolism and targeting. Nanoparticle systems are commonly designed towards receptor mediated transport and nanoparticles with proper ligands for blood-brain barrier targeting have been shown to cross the barrier with no apparent damage to the tissue. Different nanoparticles for use as drug carriers have been investigated, including polymer nanoparticles, liposomes, and inorganic systems, such as silica-based nanoparticles and magnetic iron oxide nanoparticles. Iron oxide/mesoporous silica nanoparticles have been demonstrated to be able to release drugs through agitation using an external magnetic field, as well as the efficacy of guidance of magnetic nanoparticles using an external

magnetic field.[4][2]



---

## 4. Iron Oxide Nanoparticle Synthesis

---

Magnetic nanoparticles have great potential for application in a large variety of fields. This includes physical applications such as data storage, but magnetic nanoparticles have also garnered interest in biomedical applications. This includes the use of magnetic nanoparticles in magnetic resonance imaging, bioseperation, biosensing, tissue engineering, hyperthermia and targeted drug delivery.[6]

### 4.1 Superparamagnetic Iron Oxide Nanoparticles

Magnetic nanoparticles, particularly the subgroup of superparamagnetic iron oxide nanoparticles offer a number of unique benefits for biomedical applications. Superparamagnetism is exhibited by nanoparticles when the dimensions of the particles are below the size of single magnetic domains of the bulk material. Superparamagnetism is characterised by alignment of magnetic moments across the entire particle. However, in the absence of an external magnetic field the direction of magnetic moments of superparamagnetic particles show high thermal fluctuations resulting in zero net magnetic moment over time and for multiple particles. This fluctuation also reduces magnetic interactions between separate superparamagnetic particles, which helps with solution stability and prevents magnetic aggregation.[6] For biomedical applications superparamagnetic iron oxide nanoparticles allow for manipulation using an external magnetic field for enrichment or separation from selected tissue. This has use in, for example, magnetic field-guided drug delivery. Additionally, through the application of an alternating magnetic field, agitation and heating of the particles can be achieved, which has unique applications as for example targeted cell death in cancer therapy.[6] Superparamagnetic iron oxide nanoparticles also has specific use in diagnosis as they can be used as contrast agents in magnetic resonance imaging. These unique properties can be utilised in parallel with the use of the nanoparticles as frameworks for surface functionalization using specific therapeutic agents. Iron oxide nanoparticles are additionally non-toxic and biodegradable.[7][8]

Different iron oxides can be synthesized as nanoparticles. Due to its magnetic properties magnetite ( $\text{Fe}_3\text{O}_4$ ) is commonly the most desirable oxide, though maghemite ( $\text{-Fe}_2\text{O}_3$ ) and hematite ( $\text{-Fe}_2\text{O}_3$ ) are also common iron oxide for nanoparticle synthesis.[7]

Several different synthesis pathways exist for the production of iron oxide nanoparticles:

physical methods such as laser ablation and high-energy ball milling, and chemical methods including co-precipitation and thermal decomposition methods. Additionally biological systems using for example bacteria have also been utilized for the synthesis of iron oxide nanoparticles.[7][6] Top-down approaches for synthesis, such as high-energy ball milling typically produces higher crystallinity samples due to processing from high crystallinity starting materials. However size and shape of particles is typically not as simple or accurate to control compared to bottom-up methods. During crystal formation in bottom-up approaches there is typically insufficient time for ideal crystal growth, the subsequent formation of which typically requires further processing.[7]

## 4.2 Hydrolysis Based Synthesis

Hydrolysis based synthesis schemes are some of the most common and simple synthesis methods. In alkaline conditions, condensation and precipitation of iron ion hydroxo complexes is initiated. For improved crystallization, precipitation of thermodynamically favorable phases can be performed. Co-precipitation of ferric ions with ferrous ions in 2:1 molar ratio is a common synthesis strategy for this purpose, though it has been showed that size and morphology of the nanostructures can be controlled by varying synthesis parameters such as the ion ratios, salt type, ionic strength, temperature as well as acidity of the solution over the synthesis. Smaller particles with narrow size range can also be synthesized using this method by utilizing micro emulsion systems.[8]

## 4.3 Thermal decomposition Based Synthesis

Thermal decomposition is another common synthesis scheme. It is characterized by the thermal decomposition of complexing agents and as such requires high temperatures. Controllable factors influencing size and morphology during synthesis is temperature, solvent and surfactants, and allows for the preparation of nanoparticles with well-controlled size and size distribution.[7]

## 4.4 Surface Functionalization

For use in biomedical application, particularly in vivo applications, iron oxide nanoparticles typically require surface functionalization. Biomedical applications require good dispersibility in harsh in vivo conditions, anti-biofouling properties for the prevention of adsorption of proteins, and of course, biocompatibility. Several different classes of coating

materials exist. These include organic polymers, organic surfactants, inorganic metals, inorganic oxides and various bioactive molecules such as peptides. Another attractive method is silica coating using an organosilane, useful due to the functionalization capabilities of the silica layer.[6]



---

## 5. Quantum Dot Synthesis

---

Quantum dots are semiconductor nanocrystals, that due to the effects of quantum confinement, which are encountered at nanoparticle sizes of around 1-10 nm, exhibit interesting and unique optical properties differing from those of the bulk material. Quantum confinement involves the confinement of exciton within the volume of the nanoparticle, similar to particle in a box systems, and with tighter confinement further separation of energy levels is exhibited. As such quantum dots represent the transition of the properties of bulk semiconductor materials, with wide continuous energy bands, to the behavior of single molecules with discrete energy levels. This behavior is exhibited clearly in quantum dot fluorescence. Comparison of for example CdSe nanoparticles with diameter of less than 2 nm with particles of diameter larger than 6 nm show a shift in fluorescence color from blue to red, showing the reduction of the bandgap. Quantum dots can be fabricated from a range of materials. Of note is the cadmium chalcogenides (CdS, CdSe, CdTe), which is typically synthesized with a wurtzite crystalline structure.[9]

### 5.1 Thermal decomposition Based Synthesis of Quantum Dots

Several different synthesis schemes exist for the production of quantum dots, though the most common are thermal decomposition methods. Similar to thermal decomposition for the synthesis of iron oxide nanoparticles, thermal decomposition for the synthesis of quantum dots involve the decomposition of molecular precursors into free monomers at high temperatures. Quantum dot synthesis differs though in the common use of “hot injection” of a room temperature precursor, typically the chalcogen. This is done to produce a sharp nucleation event, which has great influence on nanoparticle characteristics.[9] Nucleation consists of succeeding an energy barrier to form a thermodynamically stable crystal nucleus for further growth. This energy barrier is shaped by the difference in the chemical potential of the crystalline phase and the dissolved phase, which is the driving force of nanoparticle and bulk material formation, and the surface tension of the particle. The surface tension is highly dependent on surfactant molecules in the solution. The surface tension of different facets of the nanocrystal can be influenced by the choice of surfactant, allowing for preferential growth in certain directions, which has significant

influence on the shape of the resulting nanostructures.[9] At the start of the nanoparticle growth the concentration of free monomers is in such excess that growth is dominated by the reaction rate of the monomers with the crystal surface. As such, the incorporation rate of monomers is proportional with surface area, and as material required for radius growth is proportional with surface area also, growth rate is independent of radius and particle distribution is invariable over time. Into the synthesis, diffusion of monomers toward the particle surface becomes a limiting factor. Additionally the vapour pressure, the rate at which the particles melt back into solution, becomes a factor. This vapour pressure is higher for smaller particles, due to higher curvature which leads to reduced binding at the surface. At a critical radius  $r^*$  the particle will have zero growth rate due to equilibrium between release and capture of free monomers. At radii smaller than  $r^*$  the growth will be negative and at higher radii the growth will be positive, and as such  $r^*$  is placed at the peak of the energy barrier for nucleation.[9] The value of  $r^*$  is mainly dependant on monomer concentration, and is influenced by reaction temperature and surface energy. The growth rate of the crystal is dependant on  $r^*$ , and has its maximum at  $2r^*$ , see figure 5.1. This means that at small values of  $r^*$  compared to the nanocrystals, the size distribution will narrow over time as smaller particles will have a higher growth rate. However when the reaction proceeds with the depletion of free monomers the value of  $r^*$  increases. When  $2r^*$  becomes larger than the smallest particles, these will experience a reduction in growth rate, and the size distribution will increase. Finally, if  $r^*$  becomes larger than particles during the synthesis, Ostwald ripening will occur where the smallest particles melt and are incorporated in the larger particles, resulting in broadening of the size distribution and reduction in overall particle concentration.[9] An initial tight distribution of particles is important for maintaining particles in a growth regime where size distribution is not deteriorated, and as such a sharp nucleation event that does not extend into diffusion controlled growth is important.[9]

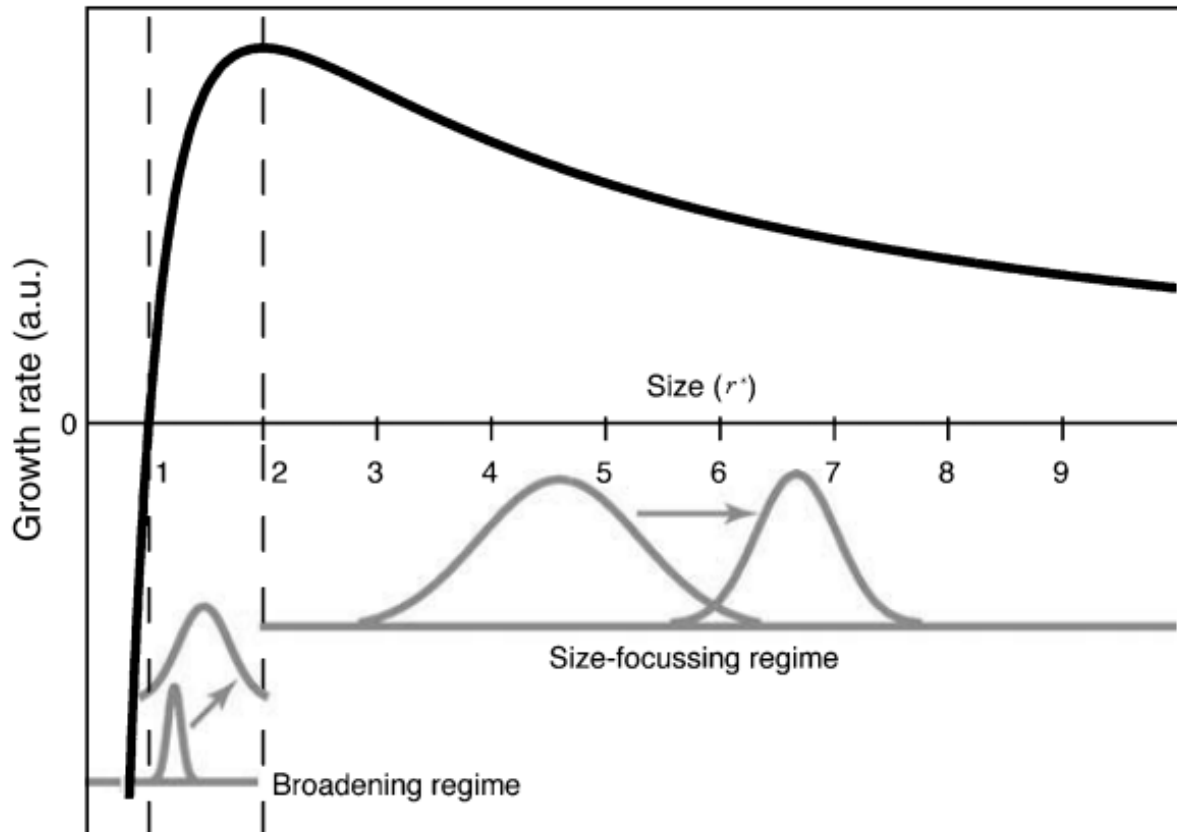


**Figure 5.1:** Graph illustrating growth regimes according to  $r^*$ . The broadening regime is marked at nanoparticle sizes smaller than  $2 r^*$ , while the broadening regime is marked at nanoparticle sizes large relative to  $r^*$ . [9]

## 5.2 Spectroscopy of Quantum Dots

Fluorescence and absorption spectroscopy can be used as a good indicator of quantum dot size and size distribution. Absorption of a photon can occur when the energy of it exceeds the band gap, with a sharp absorption peak at its onset. The form and width of this peak is dependent on size distribution as well as particle form and stoichiometry. Similarly, fluorescence in the semiconductor can occur after absorption of a photon, resulting in excitation to the conduction band and subsequent emission of light corresponding to the difference between the lowest energy state in the conduction band and the valence band. The width of the fluorescence spectrum similarly corresponds to the size distribution, with samples with tight distribution exhibiting widths in the range of 20-25 nm FWHM. The emission peak for quantum dots is red-shifted by approximately 10-20 nm compared to the absorption peak, which is a phenomenon known as Stokes-shift. [10]

### 5.3 Shell Formation

A common scheme for the modification of quantum dots is the formation of a shell around the dot, consisting of a second semiconductor. For successful shell growth, lattice mismatch must be limited, and is typically accomplished with slow addition of precursors at relatively low temperatures. Significant improvement of the optical properties, including quantum yield and reduced blinking, results from the shell in some cases serving to passivate the surface of the quantum dot, separating it from the surrounding environment.[10]

---

## 6. Materials and Methods

---

In the following chapter the materials and methods used will be presented.

### 6.1 Co-Precipitation Synthesis of Iron oxide Nanoparticles

Synthesis of iron oxide nanoparticles by co-precipitation was based on a modified protocol.[11] Synthesis was done as well as silica coating of the particles. The materials and methodology of this is described in the following.

#### 6.1.1 Materials

The following table lists the materials used in the co-precipitation synthesis of iron oxide nanoparticles and silica coating of iron oxide nanoparticles.

Chemicals	Lot nr.
Iron(III) chloride hexahydrate	80730
Iron(II) sulfate heptahydrate	128422 22706182
Ammonium hydroxide	S45436-487
Sodium citrate	28H0209
Oleic acid	27728
TEOS	0001423504

#### 6.1.2 Method

For iron oxide nanoparticles, 2.5 ml 0.2M Iron(III) chloride hexahydrate and 10 ml 0.1 M Iron(II) sulfate heptahydrate was diluted to 100 ml with MQ water. Under nitrogen flow and vigorous stirring 20 mL 2M ammonium was added at a rate 3ml/min. 10 min after base addition 2g sodium citrate was added. The particles were subsequently washed by precipitating using ethanol and resuspending in MQ water, which was repeated 3 times.

#### Silica Coating of Iron Oxide Nanoparticles

Silica coating of iron oxide nanoparticles was attempted to test a silica coating protocol.[3]

Following synthesis of iron oxide nanoparticles stabilization was replaced from citrate to oleic acid. This was done by adding to 2ml of the iron oxide suspension a gross excess of oleic acid and agitating the phases for approximately 16 hours. The particles were then precipitated by centrifugation and resuspended in ethanol. This was repeated twice to ensure removal of water from the solution.

Silica shell coating was performed on the ethanol suspended nanoparticles. For coating, 2 mg iron oxide nanoparticles in 20 mL ethanol under vigorous stirring were added 3 ml MQ water and 1 ml ammonium solution dropwise and following this 50  $\mu$ l TEOS. This solution was stirred for 20 min and the particles were subsequently isolated by centrifugation and resuspended in 8 ml MQ water. Resuspension, in 2ml MQ, was repeated to wash the particles.

## 6.2 Thermal decomposition synthesis of Iron oxide nanoparticles

Iron oxide nanoparticles were also synthesized using a thermal decomposition method.[3] The materials and methodology is described in the following.

### 6.2.1 Materials

The following table lists the materials used in the thermal decomposition synthesis of iron oxide nanoparticles.

Chemicals	Lot nr.
Iron(III) chloride hexahydrate	80730
Oleic acid	27728
NaOH	
Hexane	MKCH5832
Chloroform	SHBJ2941
Octadecene	MKBD0024
Methanol	SHBC9010V

### 6.2.2 Methods

Sodium oleate was synthesised by saponification of oleic acid. This was done by addition of 0.71g sodium hydroxide to 5.56ml oleic acid dissolved in 50 ml ethanol. This solution was stirred at room temperature for approximately 16 hours after which the solvent was removed using a rotary evaporator.

Iron oleate was subsequently synthesised.[12] 10.8 g iron(III) chloride hexahydrate and 36.5 g of sodium oleate was dissolved in a solvent mixture of 80 ml ethanol, 60 ml MQ water and 140ml hexane. The solution was heated to 70 °C and refluxed for four hours. Subsequently the organic layer was separated and washed three times with 30 ml MQ water using a separatory funnel. Subsequently the hexane was evaporated using a vacuum desiccator.

Iron oxide nanoparticles were synthesized using a mixture of 900 mg iron oleate, 190  $\mu$ l oleic acid and 5 ml octadecene, in a three necked round bottom flask. This mixture was heated under nitrogen flow to boiling temperature and was kept boiling for one hour. The resulting particles were precipitated using acetone and redispersed in chloroform, precipitating with an external magnet. The particles were subsequently washed repeatedly using acetone and methanol for precipitation, and redispersing in chloroform.

## 6.3 Thermal Decomposition Synthesis of Quantum dots

CdSe quantum dots were synthesized by thermal decomposition using two different methods, referred to as method 1[13] and method 2.[3] The materials and methodology is described in the following.

### 6.3.1 Materials

The following table lists the materials used in the thermal decomposition synthesis of quantum dots.

Chemicals	Lot nr.
Se	209651-50G
Trioctylphosphine	13403PC
Octadecene	MKBD0024
CdO	
Oleic acid	27728
Octadecylphosphonic acid	SHBC9019V
Trioctylphosphine oxide	Q3LIB-EL
Hexane	MKCH5832
Methanol	SHBC9010V

### Method 1

Firstly, a solution of selenium was made by adding 30 mg Se and 0.4 ml trioctylphosphine to 5 ml octadecene while heating and stirring. For the synthesis 13 mg of CdO was added to a 100 ml three necked round bottom flask along with 0.6 ml oleic acid and 10 ml octadecene. The mixture was heated using a thermowell to 225 °C after which 1 ml of the room temperature selenium solution was added to the mixture to start the synthesis. Two variations of the synthesis was done at this point. An initial experiment was conducted where 1 ml samples were removed over a period of 30 min. Based on size estimates from these samples, subsequent syntheses were terminated after a specific time by cooling the flask in ice. The particles were subsequently precipitated using acetone and centrifuging. The particles were resuspended in hexane and washed by precipitating with either acetone, methanol or both and resuspending in chloroform.

### Method 2

Firstly, the selenium solution was prepared by adding 60 mg Se to 0.5 ml trioctylphosphine and stirring the solution for approximately 16 hours. For the synthesis, 60 mg CdO, 280 mg octadecylphosphonic acid and 3 g trioctylphosphine oxide was added to a 100 ml three necked round bottom flask. This mixture was degassed under vacuum while heating to 150 °C in a thermowell for 1 hour. For some syntheses the mixture was left to rest at this point. The mixture was subsequently heated to 320 °C under nitrogen, at which point 1 ml trioctylphosphine was added to the mixture. The temperature was raised to 380 °C and the synthesis started by the addition of the selenium solution. Similar to the first synthesis method, an initial experiment was conducted to ascertain size dependence on reaction time. The reaction was terminated by transferring the mixture to a container on ice. The solid cooled synthesis product was either dissolved in hexane and subsequently precipitated using acetone and resuspended in hexane, or directly precipitated using acetone, resuspending in hexane. The particles were further washed by precipitation using either acetone, methanol or both.

## 6.4 CdS Shell Synthesis

CdS Shell Synthesis was done for both quantum dot synthesis methods.[14] The materials and methodology is described in the following.

### 6.4.1 Materials

The following table lists the materials used in the CdS shell synthesis.

Chemicals	Lot
Oleic acid	27728
CdO	
Octadecene	MKBD0024
Oleylamine	0C2JA HM
Octanethiol	KS3OH-KL
Methanol	SHBC9010V
Chloroform	SHBJ2941

Firstly, cadmium oleate was synthesized.[15] This was done by combining 4.550 g oleic acid and 0.518 g CdO. The mixture was degassed at 100 °C and then heated to 190 °C under nitrogen flow for 10 min. Subsequently the solution was cooled to 110 °C and degassed for 20 min. Acetone was added to precipitate the cadmium oleate, which was precipitated by centrifugation, washed with acetone, and subsequently dried using a vacuum desiccator.

100 nmol of CdSe quantum dots in hexane solution were used as cores for coating. The molarity of solution for the first method was determined based on dry weight, due to loss during initial precipitation, while molarity for the second method was based on the limiting reactant of the synthesis. The quantum dots were loaded in a solution mixture of 3 ml octadecene and 3 ml oleylamine. The mixture was degassed under vacuum at room temperature for one hour and 120 °C for 20 min. Subsequently the mixture was heated 240 °C in a thermowell under nitrogen flow, at which point a desired amount of cadmium oleate and 1.2 times an equivalent amount of octanethiol diluted in 12 ml octadecene, was injected into the flask at a rate of 3 ml/hour using a syringe pump or funnel drip. The amount of cadmium oleate was based on a target diameter of 7.4 nm for particles synthesized using method 1 and 9nm for particles synthesized using method 2. After injection 1 ml oleic acid was added to the flask and the mixture was further annealed 310 °C for 60 min. The produced particles were precipitated by adding acetone and redispersed in ethanol. The particles were washed by precipitation and redispersion using either acetone or acetone and methanol, and redispersed in chloroform.

## 6.5 Supernanoparticle Synthesis

Supernanoparticles were synthesized using different combinations of washed and unwashed quantum dots, synthesized through both methods, with and without CdS shell and iron

oxide nanoparticles, synthesized through thermal decomposition. The materials and methodology is described in the following.[3]

### 6.5.1 Materials

The following table lists the materials used in the supernanoparticle synthesis

Chemicals	Lot nr.
Chloroform	SHBJ2941
Dodecyltrimethylammonium bromide	440003/1 22807060
PVP(55k molecular weight)	MK BK0843V
Ethylene glycol	02760

### 6.5.2 Methods

Quantum dots and iron oxide nanoparticles in 1 ml chloroform were injected into a 1 ml 20 mg/ml dodecyltrimethylammonium bromide MQ solution. The solution was vortexed to form a micelle suspension and nitrogen was blown into the mixture to remove the chloroform. The micelle suspension was injected into 5 ml 2mM PVP(55k molecular weight) ethylene glycol solution under vigorous stirring. The mixture was stirred for 30 min at a speed of 750 rpm. The particles were subsequently isolated using either an external magnet or by centrifugation, using 10000rcf for 30min, and were redispersed in ethanol.

---

## 7. Results

---

In the following chapter the results of experiments conducted during the project will be presented.

### 7.1 NTA measurements of Iron Oxide Nanoparticles

Iron oxide nanoparticles were synthesized using a co-precipitation method. To evaluate the size of synthesized nanoparticles NTA was performed, see figure 7.1. Size evaluation using NTA was also performed on the particles where silica coating was attempted, see figure 7.1.

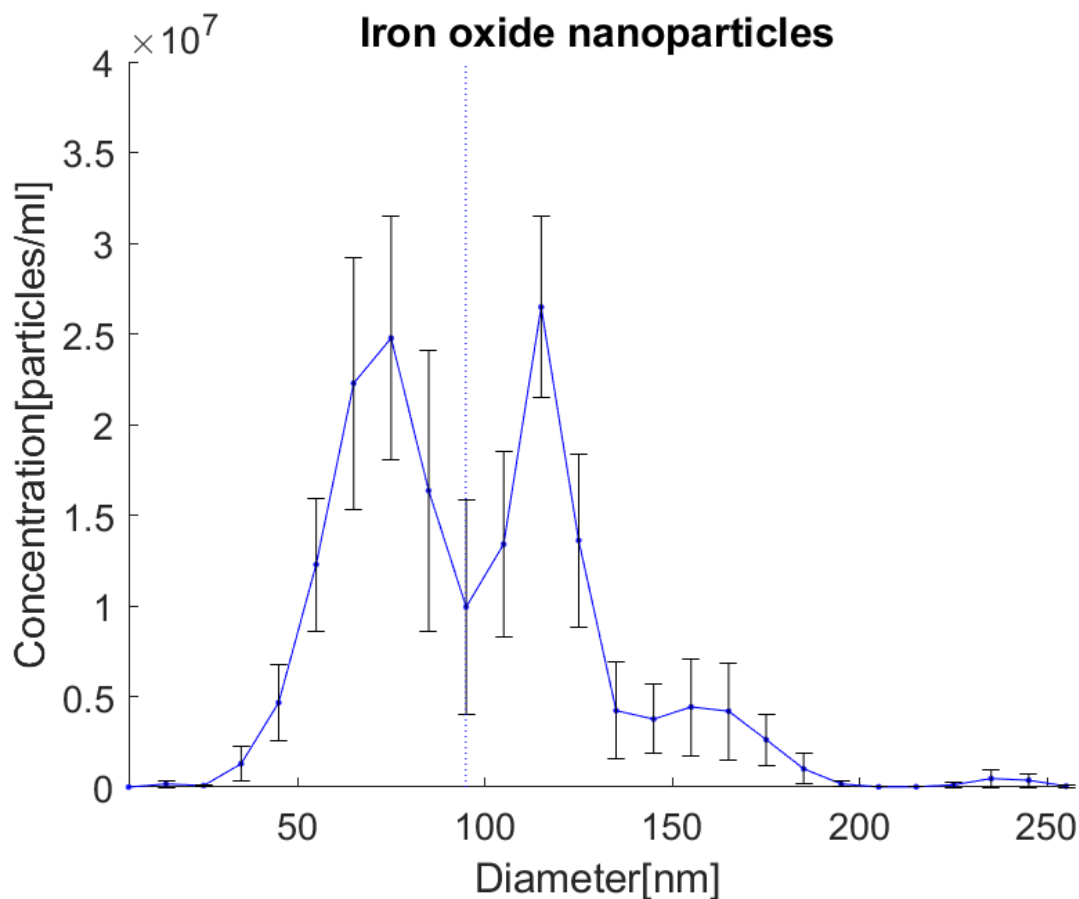


**Figure 7.1:** NTA measurements of Iron oxide nanoparticles synthesized through a co-precipitation method. The blue dotted line marks the mean size at 81.2nm with a standard error of 17.7nm.

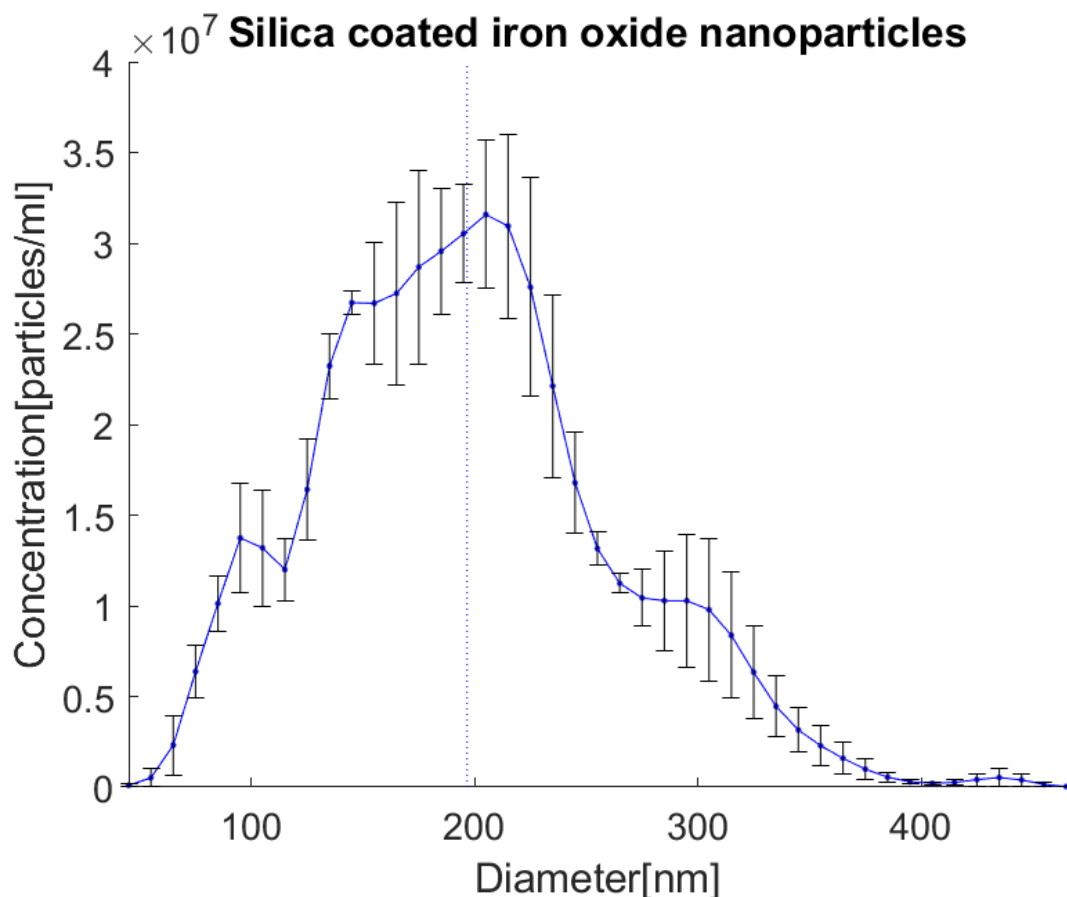


**Figure 7.2:** NTA measurements of Iron oxide nanoparticles synthesized through a co-precipitation method and coated with a silica shell. The blue dotted line marks the mean size at 188.7nm with a standard error of 24.4nm.

The NTA measurements for both samples show relatively polydisperse particles, with sizes ranging from approximately 50nm to 200nm for the uncoated, and 50nm to 400nm for the coated. Additionally, a significant increase in the mean particle size can be observed, from 81.2nm with a standard error of 17.7nm to 188.7nm with a standard error of 24.4nm.

## 7.2 SEM Imaging of Iron Oxide Nanoparticles

To further elucidate the nanostructure of the Iron oxide nanoparticles, SEM imaging was performed. SEM images were taken of the iron oxide nanoparticles, figure 7.3 and 7.4, iron oxide nanoparticles after the stabilizer was changed to oleic acid, figure 7.5 and 7.6 and post silica coating particles, figure 7.7 and 7.8.

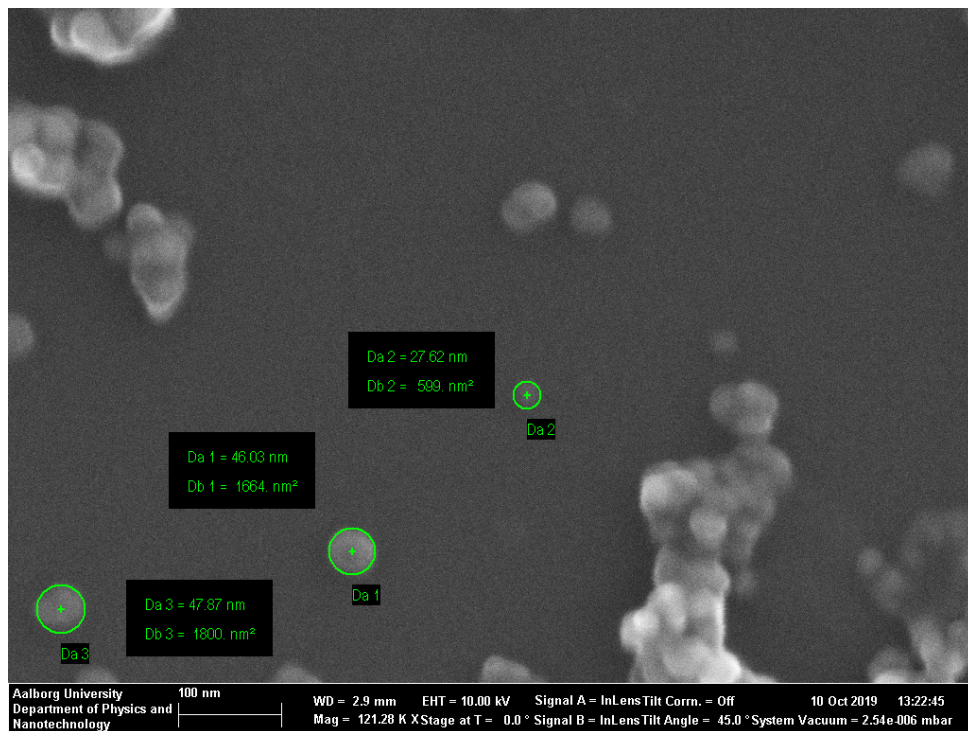


**Figure 7.3:** SEM image of uncoated, citrate stabilized iron oxide nanoparticles. Marked particles have diameters of 27.62nm, 46.03nm and 47.87nm

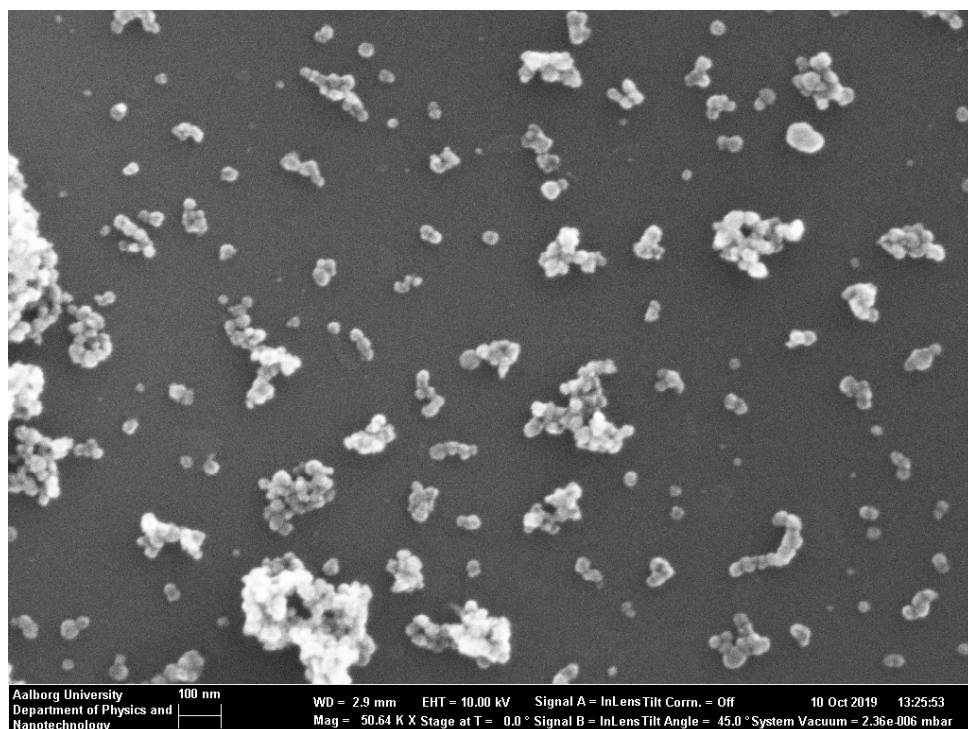


**Figure 7.4:** SEM image of uncoated, citrate stabilized iron oxide nanoparticles.

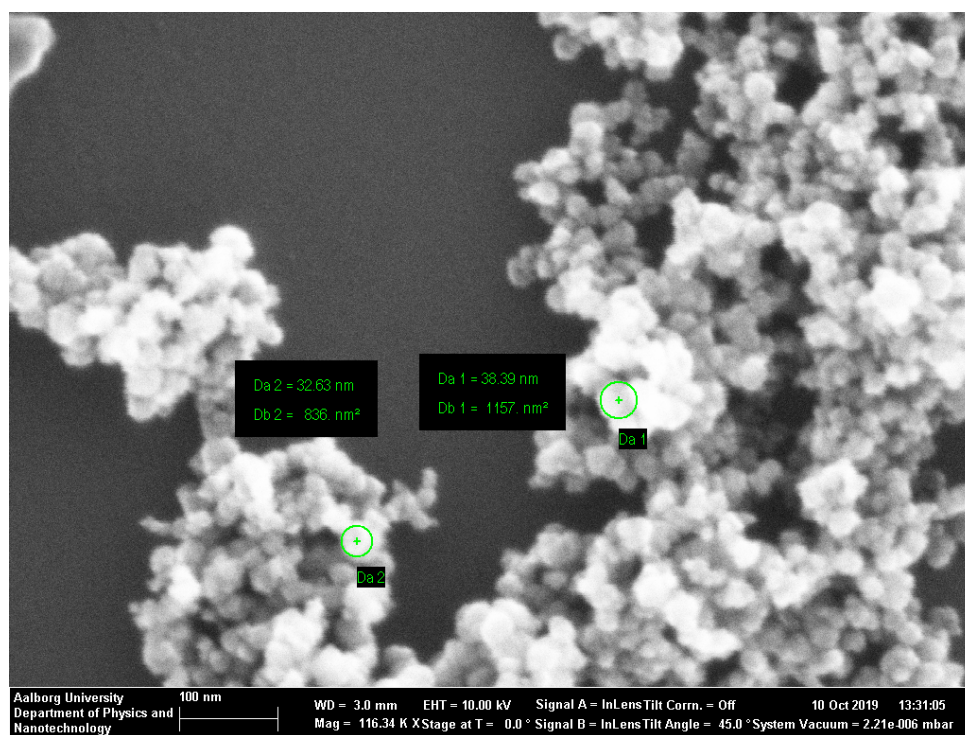


**Figure 7.5:** SEM image of uncoated, oleic acid stabilized iron oxide nanoparticles. Marked particles have diameters of 32.63nm, 38.39nm

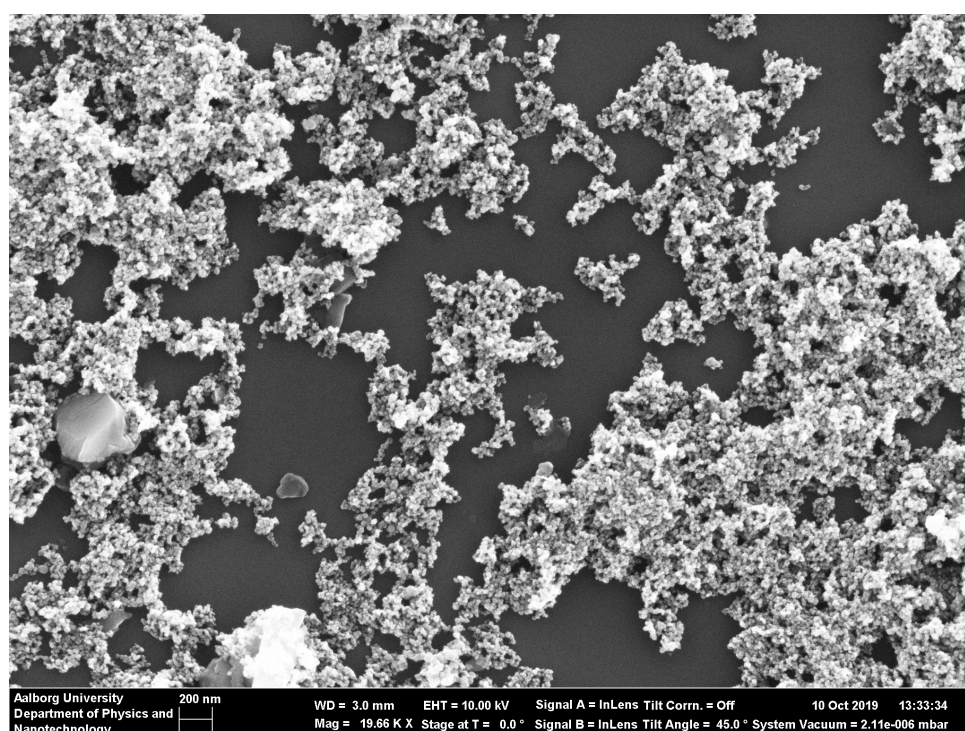


**Figure 7.6:** SEM image of uncoated, oleic acid stabilized iron oxide nanoparticles.

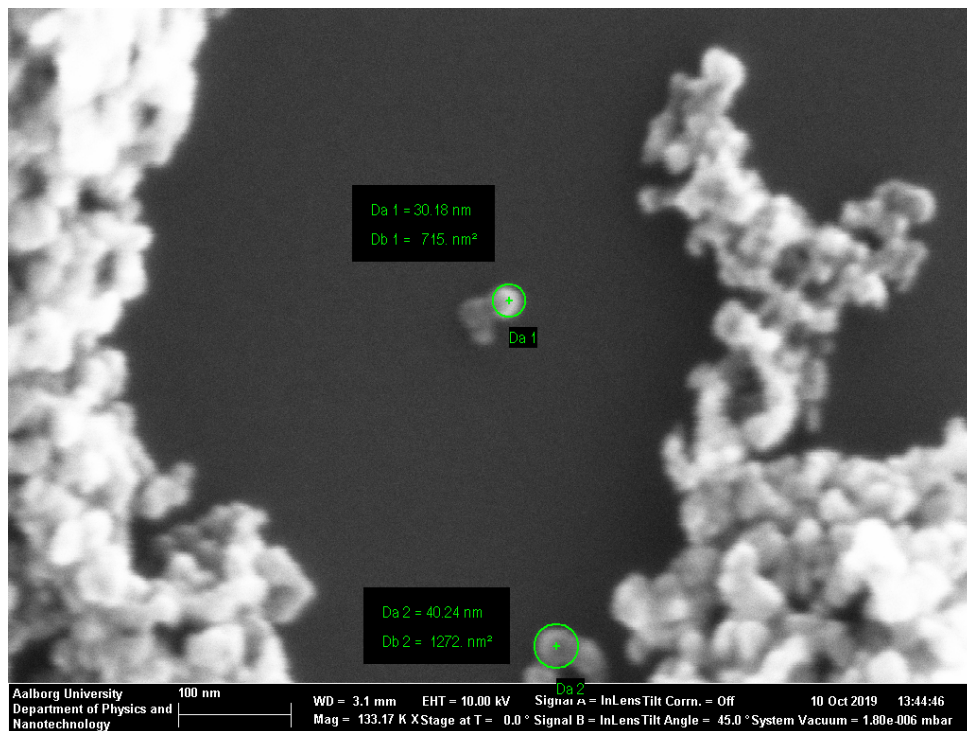


**Figure 7.7:** SEM image of silica coated iron oxide nanoparticles. Marked particles have diameters of 30.18nm and 40.24nm

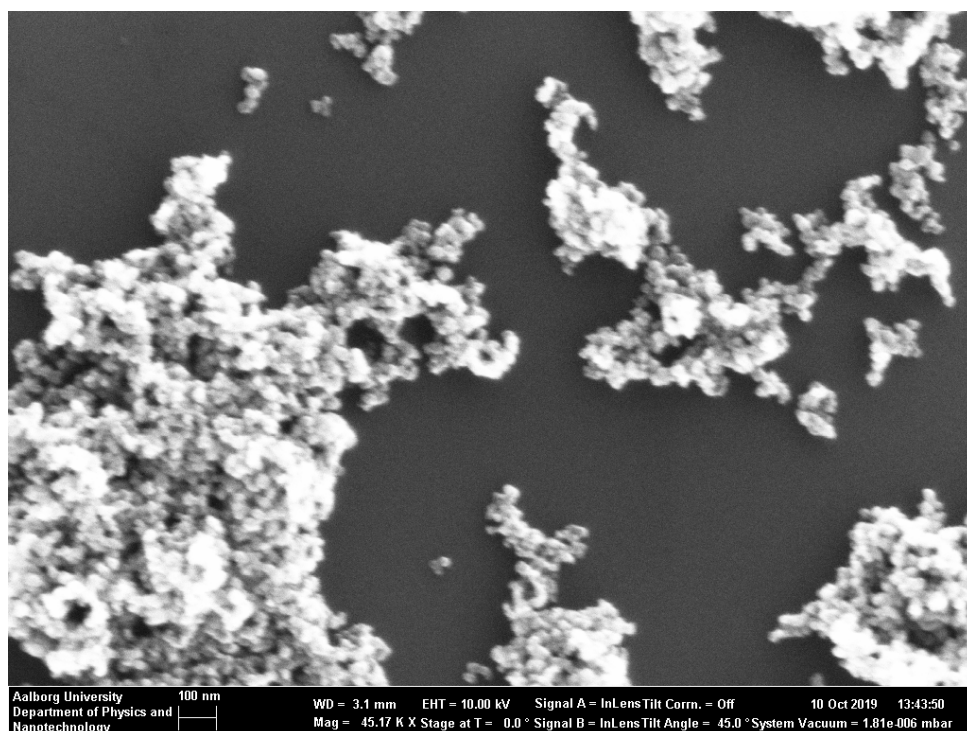


**Figure 7.8:** SEM image of silica coated iron oxide nanoparticles.

From the SEM images, the iron oxide nanoparticles can be seen to have diameters in the range around 25nm to 50nm. Aggregates of multiple particles are prevalent along

with single particles and aggregates of few particles. SEM images of oleic acid stabilized particles and silica coated particles show exclusively aggregates of many particles. Individual particles in the aggregates are in a similar size range as the uncoated particles.

### 7.3 DLS measurements of Iron Oxide Nanoparticles

Iron oxide nanoparticles were also synthesized using a thermal decomposition method. These particles were characterised using DLS, due to the solvent and size limitations of NTA. The results of the DLS measurements are shown in figure 7.9 and 7.10.

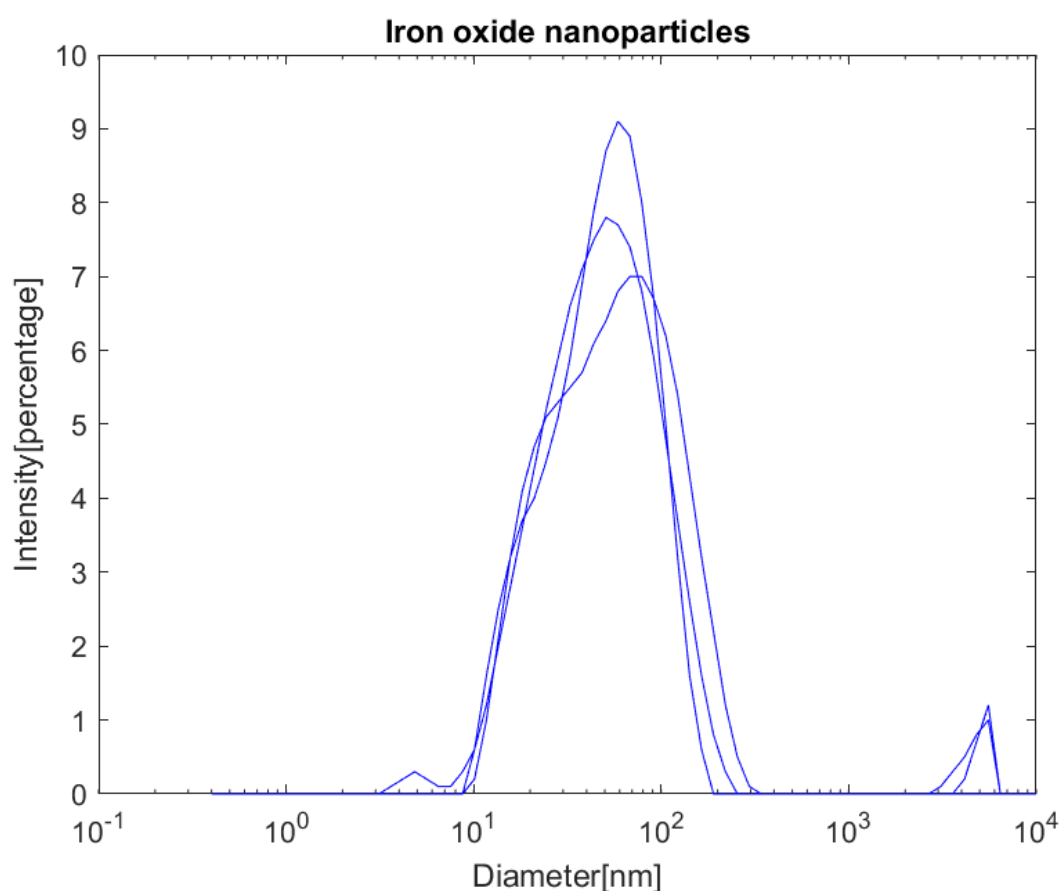


**Figure 7.9:** DLS intensity measurements of iron oxide nanoparticles synthesised through thermal decomposition.

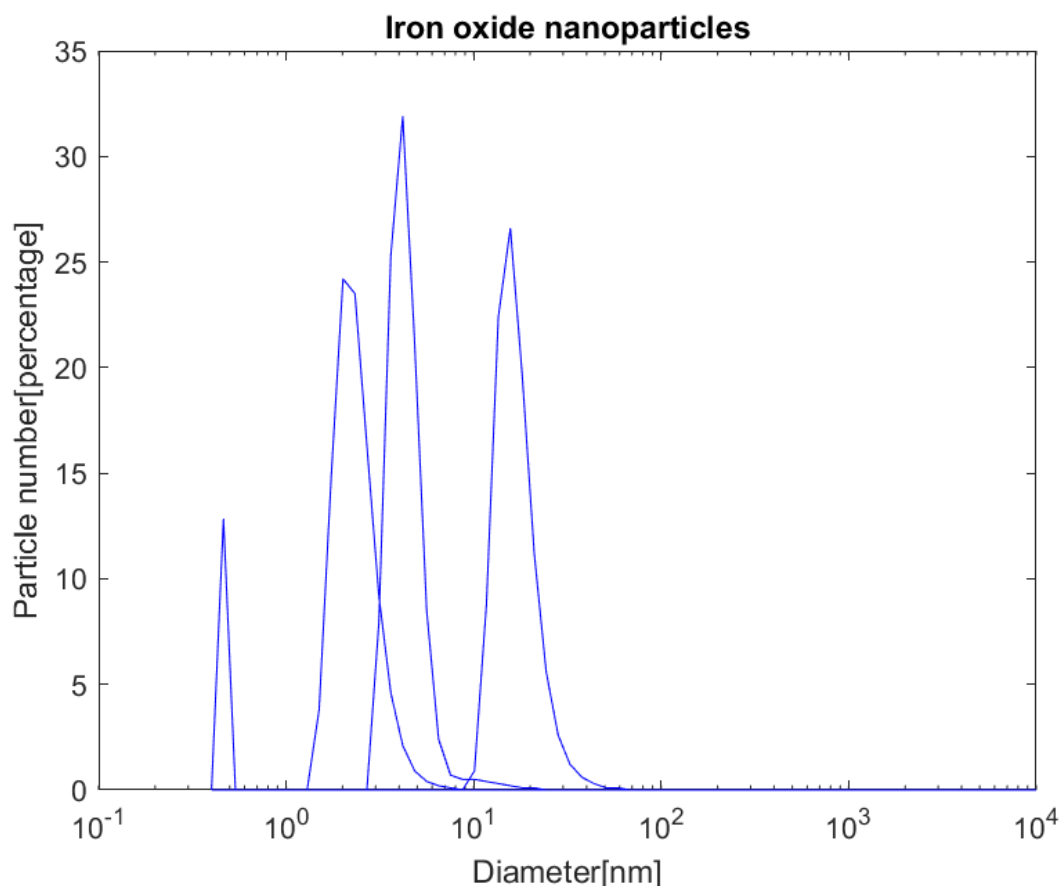


**Figure 7.10:** Number transformation of DLS measurements of iron oxide nanoparticles synthesised through thermal decomposition. Peak sizes are 4.2nm, 15.7nm and 2.0nm

The DLS intensity measurements show the presence of particles with sizes between approximately 10nm to 200nm with small peaks at less than 10 nm and at approximately 5000nm. The number transformation of these same measurements show narrow but scattered peaks at 4.2nm, 15.7nm and 2.0nm.

## 7.4 Absorption Spectroscopy Measurements of Quantum Dots

Quantum dots were synthesized through two different thermal decomposition methods. Each synthesis was initially calibrated through an initial experiment to evaluate the size dependence on reaction time. For the first method, samples were collected after a period of 30s, 1min, 1min 30s, 2min, 3min, 5min, 10min, 15min, 20min and 30min, the absorbance graphs of which can be seen in figure 7.11. For the second method, samples were collected after 20s, 45s, 1min 30s, 2min, 4min, 8min, the absorbance graphs of which can be seen in figure 7.12.

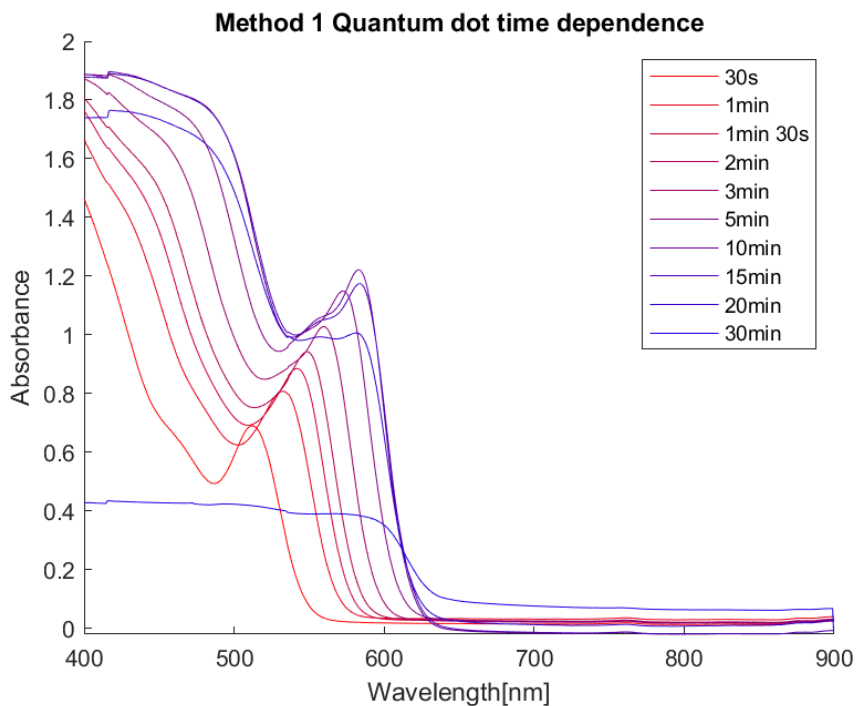


**Figure 7.11:** Absorbance measurements of the initial experiment to determine size dependence of quantum dots of synthesis method 1.

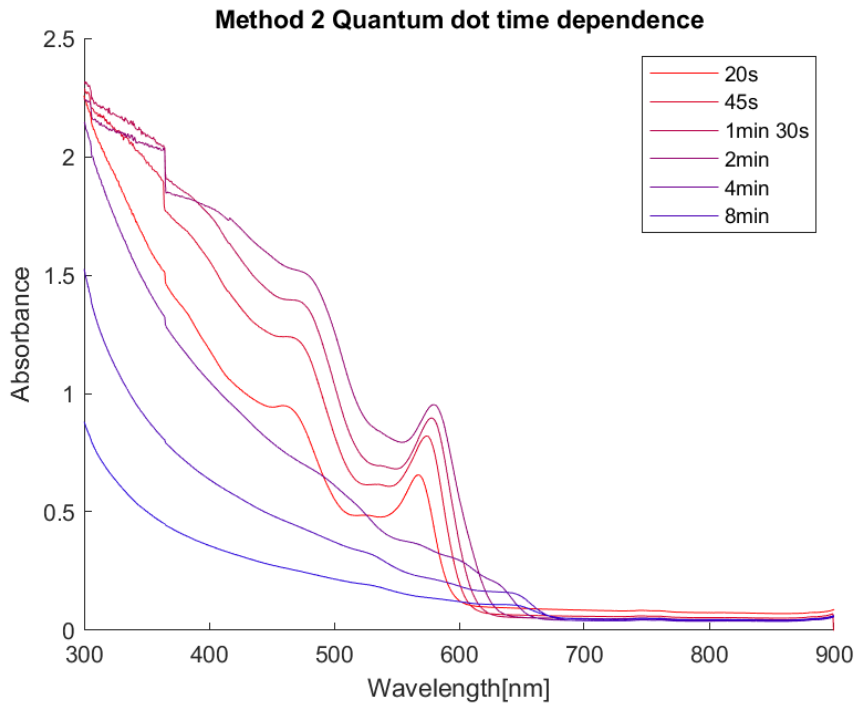


**Figure 7.12:** Absorbance measurements of the initial experiment to determine size dependence of quantum dots of synthesis method 2.

For particles synthesized through method 1, the first absorption peaks can be seen shift-

ing to the higher wavelengths as the reaction time increases, until 10min at which point the peaks remain at the same wavelength. For the 20min measurement, the absorbance starts to lose its characteristics, while the 30 min measurement has lost most absorbance features and significantly flattened at lower wavelengths.

For particles synthesised through method 2, the absorption peaks show only small shifts to higher wavelengths for the first four measurements. Additionally the loss of absorbance characteristics is lost significantly earlier at the 2min measurement.

Quantum dot size was calculated according to formula 7.1.[16]

$$D = (1.6122 \cdot 10^{-9})\lambda^4 - (2.6575 \cdot 10^{-6})\lambda^3 + (1.6242 \cdot 10^{-3})\lambda^2 - (0.4277)\lambda + (41.57) \quad (7.1)$$

The calculated size development with reaction time for both method 1 and 2 can be seen in figure 7.13 and figure 7.14, respectively.

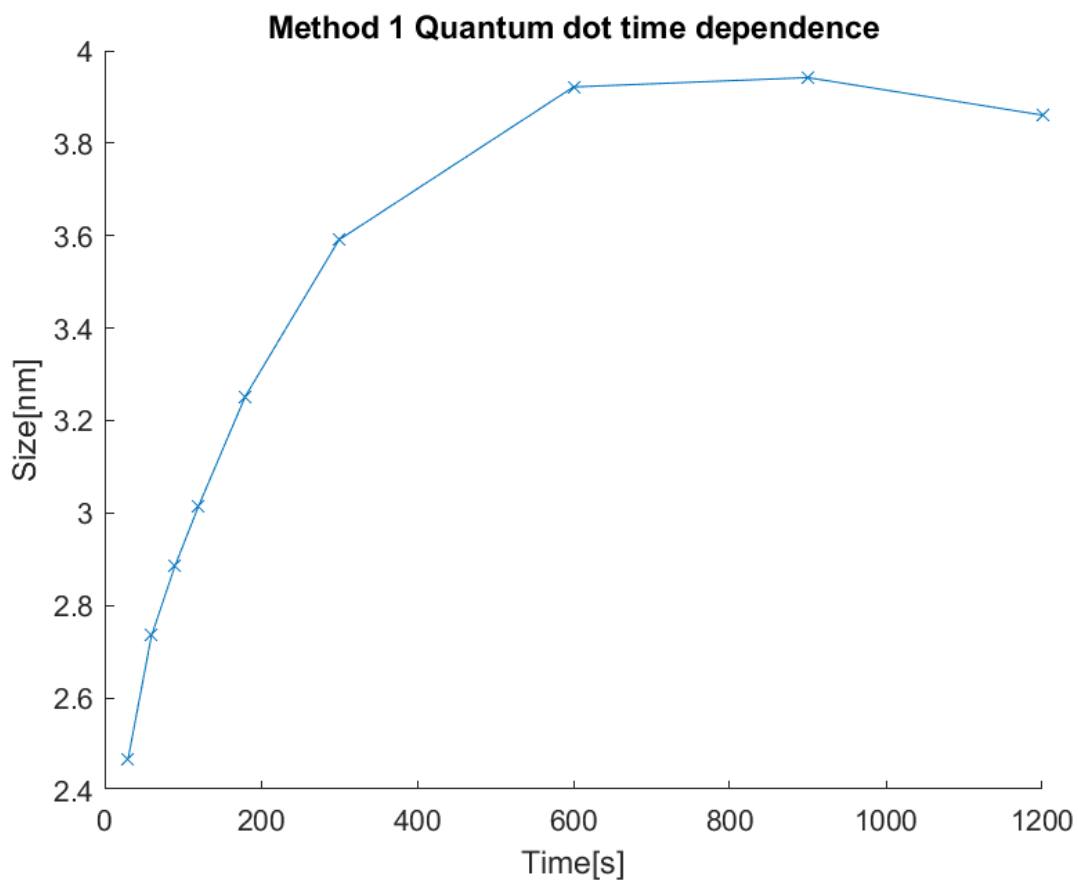


**Figure 7.13:** Size development with reaction time for quantum dots synthesized through method 1.

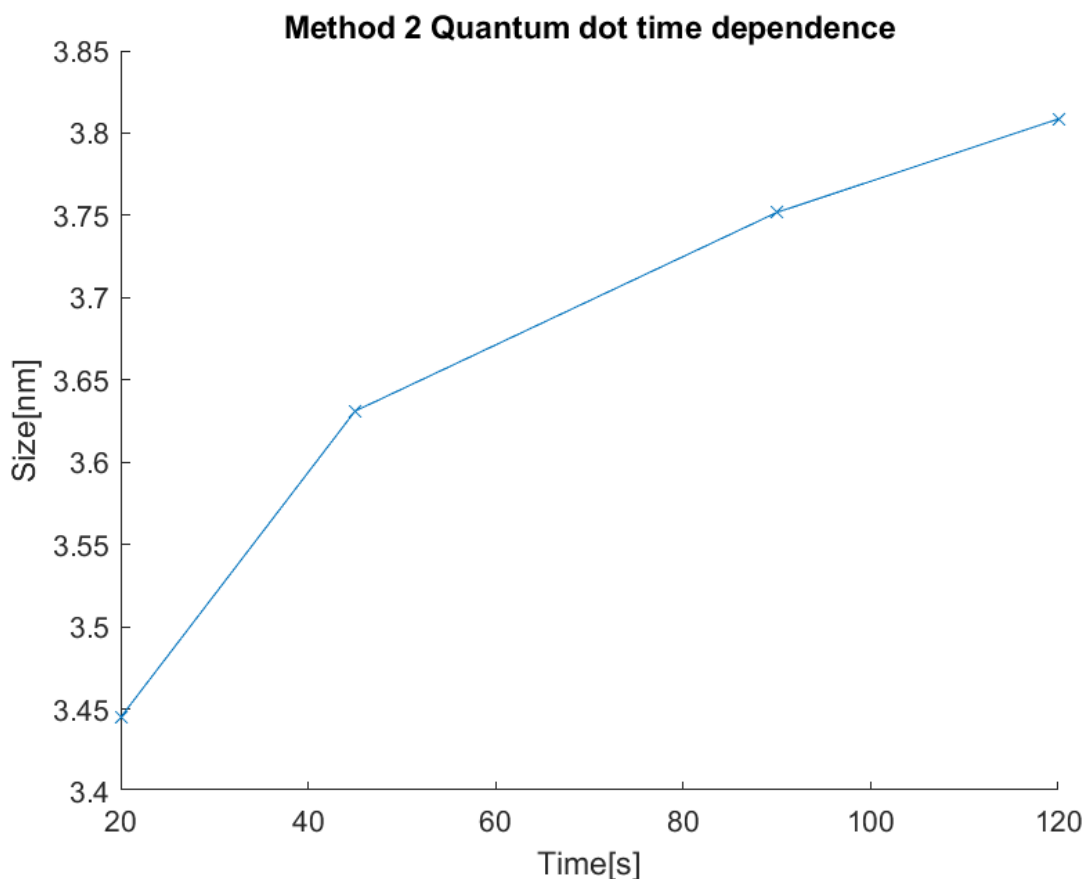


**Figure 7.14:** Size development with reaction time for quantum dots synthesized through method 1.

For the first method, quantum dot size increases quickly at the start of the synthesis at approximately 2.4nm, and reaches a maximum after 10min at a size around 4nm, with no further development in quantum dot size.

For the second method, nanoparticle size at 20s starts at 3,45nm and only increases a little to around 3.8nm after 120s.

Stock synthesis of quantum dots using the first method was performed with a reaction time of 10min and resulted in a first peak wavelength of 579nm corresponding to a size of 3.8nm. Other stock preparations were synthesized. However these exhibited significantly worse fluorescence. This was due to the use of Selenium solutions that had either been stored for too long and deteriorated, or Se solutions that had been prepared at too high temperatures, and were largely discarded.

Stock synthesis using the second method was performed with a reaction time of 45s. Stock synthesis was performed multiple times for the second synthesis due to results differing from the initial experiment. In the following table the synthesized nanoparticle sizes for

the different samples are listed, as well as the modifications to the synthesis methodology for these samples.

Stock number	Experimental conditions	Peak wavelenth and Particle Size
0	Initial experiment. The particles were left to rest for two days after degassing.	574nm 3.6nm
1	First Stock synthesis. No rest after degassing.	613nm 5.3nm
2	Significant attempts to keep oxygen from the synthesis after degassing and injection, resulting in increased loss of solvent due to nitrogen flow.	596nm 4.4nm
3	Reduced nitrogen flow to reduce solvent loss during synthesis.	No absorbance peak
4	Double solvent used in preperation of Se solution. Nitrogen flushed during degassing.	562nm 3.3nm
5	Particles were left to rest for one day after degassing.	545nm 2.9nm

## 7.5 Fluorescence Spectroscopy Measurements

Fluorescence measurement were made to characterize the quantum dots as well as the further modifications of these. Peak emission wavelength and FWHM values for stock syntheses using quantum dot synthesis method 2 were measured and are displayed in the following table:

Stock number	Fluorescence emission peak wavelength	FWHM
1	620	25
2	603	26
3	644	60
4	580	34
5	563	37

Peak emission wavelength for these particles are slightly above the values of first peak absorption wavelength. Additionally for the third stock solution, a high peak emission wavelength can be observed. FWHM measurements are lower for the first 2 stock preparations at 25nm and 26nm, and higher for the fourth and fifth at 34nm and 37nm. FWHM is significantly higher for the third stock preparation, at 60nm, than the other samples.

Fluorescence measurements were also made on quantum dots with a CdS shell. Graphs of the fluorescence measurements for the first synthesis stock is shown in figure 7.15 and figure 7.16 for particles with and without CdS shell, respectively.

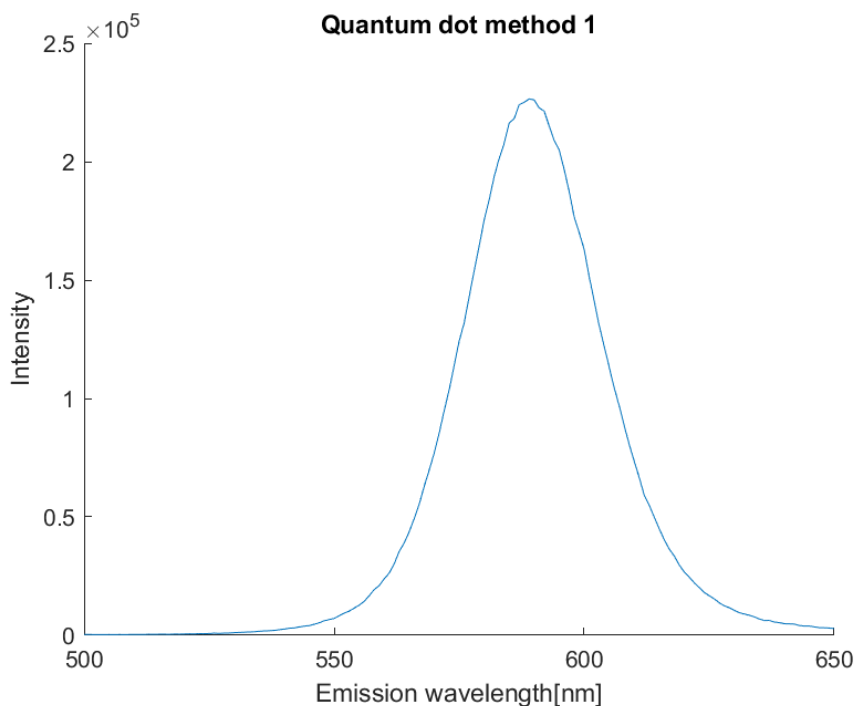


**Figure 7.15:** Fluorescence emission measurement of quantum dots synthesized using method 1. Peak wavelength is at 589nm and FWHM is at 33nm. Excitation wavelength of 490nm.

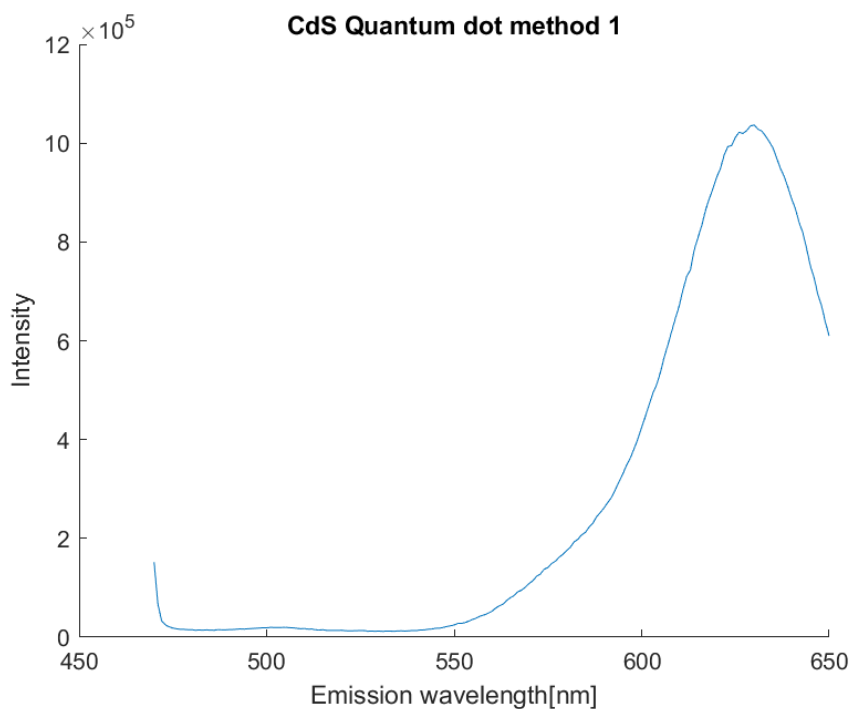


**Figure 7.16:** Fluorescence emission measurement of quantum dots with CdS shell synthesized using method 1. Peak wavelength is at 630nm and FWHM(based only on intersection on the left) is at 52nm. Excitation wavelength of 460nm.

The fluorescence after CdS shell formation is shifted significantly from 589nm to 630nm. Additionally the FWHM measurement is increased from 33 nm to 52nm, with the measurement of FWHM for CdS shell particles based on the left intersection.

For quantum dot synthesis method 2, CdS shell formation was performed on stock 5. The fluorescence emission graph for particles with and without shell coating are shown in figure 7.17 and 7.18, respectively.

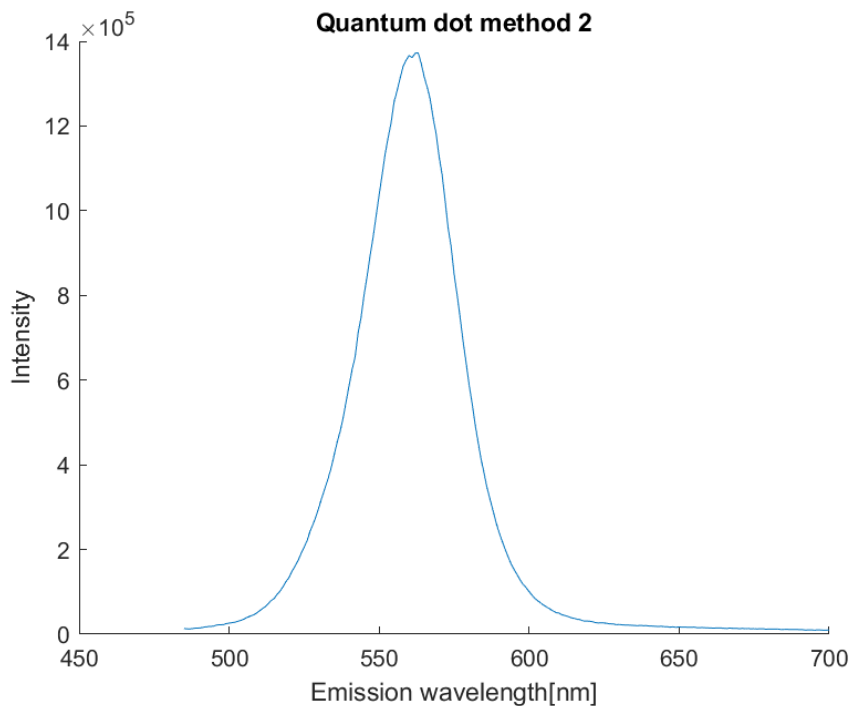


**Figure 7.17:** Fluorescence emission measurement of quantum dots synthesized using method 2. Peak wavelength is at 563nm and FWHM is at 37nm. Excitation wavelength of 475nm.

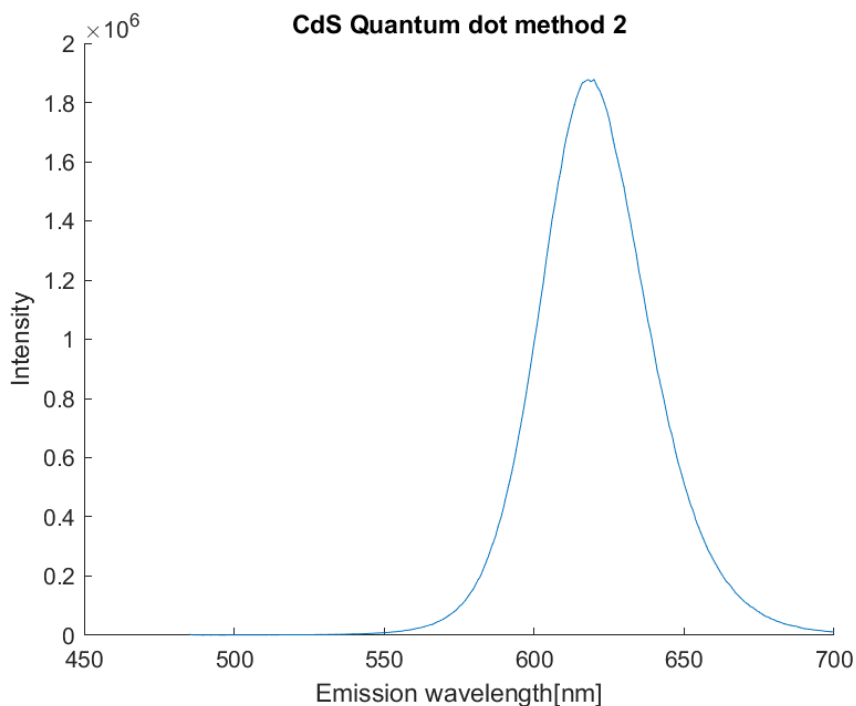


**Figure 7.18:** Fluorescence emission measurement of quantum dots with CdS shell synthesized using method 1. Peak wavelength is at 618nm and FWHM is at 42nm. Excitation wavelength of 475nm.

Similar to particles synthesized using method 1, peak absorption wavelength is increased after CdS shell formation, from 563nm to 618nm. Also, FWHM for the peak is increased from 37nm to 42nm.

Fluorescence measurements were also done to evaluate supernanoparticle synthesis. Several different combinations of different quantum dots and iron oxide nanoparticles, using different washing methods, was attempted. Only iron oxide nanoparticles synthesized through thermal decomposition was used for supernanoparticle assembly. Supernanoparticle assembly using iron oxide nanoparticles without repeated washing in acetone and methanol resulted in the failure of particles to be dispersible in ethanol after synthesis. Synthesis using quantum dots synthesized using method 2 without CdS shell also resulted in particles unable to disperse in ethanol. Using washed iron oxide nanoparticles and washed quantum dots synthesized using method 1, a dispersion could be prepared, though without fluorescence. Fluorescent, dispersible particles could be synthesized using quantum dots with CdS shell, though particles based on the method 2 synthesis had to be cleaned using acetone and not methanol to produce fluorescent particles. Fluorescence measurements were performed for three variations of the synthesis, each using washed iron oxide nanoparticles and washed quantum dots, synthesized using method 2, with CdS shells. SP1 using 4mg quantum dots and 6mg iron oxide nanoparticles in the synthesis, See figure 7.19. SP2 using 9mg quantum dots and 6mg iron oxide nanoparticles in the synthesis, see figure 7.20. And finally SPC using 4mg quantum dots and 6mg iron oxide nanoparticles and using centrifugation for precipitation instead of a magnet, see figure 7.21.

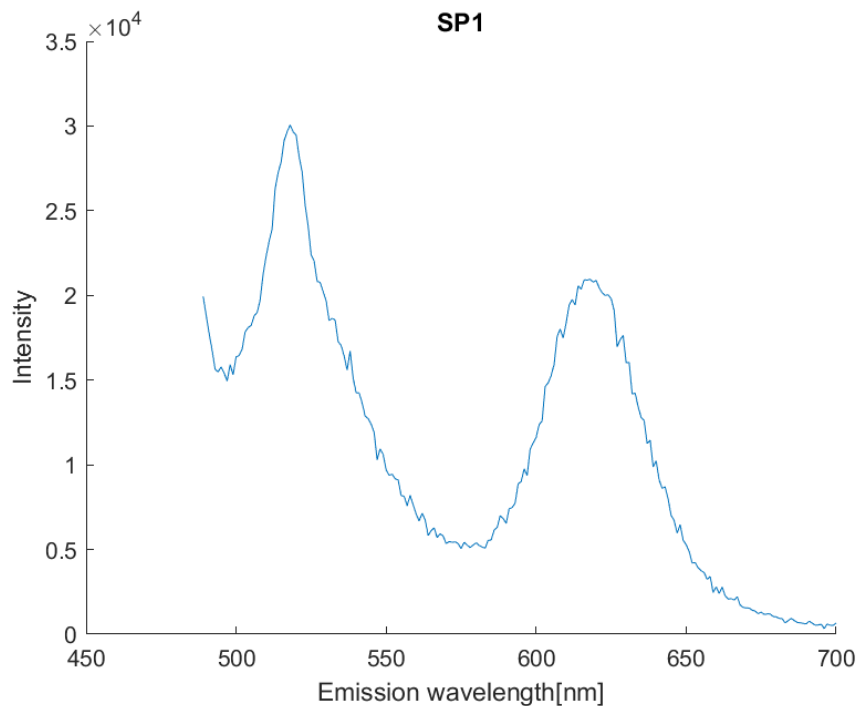


**Figure 7.19:** Fluorescence emission measurement of super nanoparticle synthesis products of SP1. Left peak wavelength is 518, right peak wavelength us 618. Excitation wavelength of 475nm.

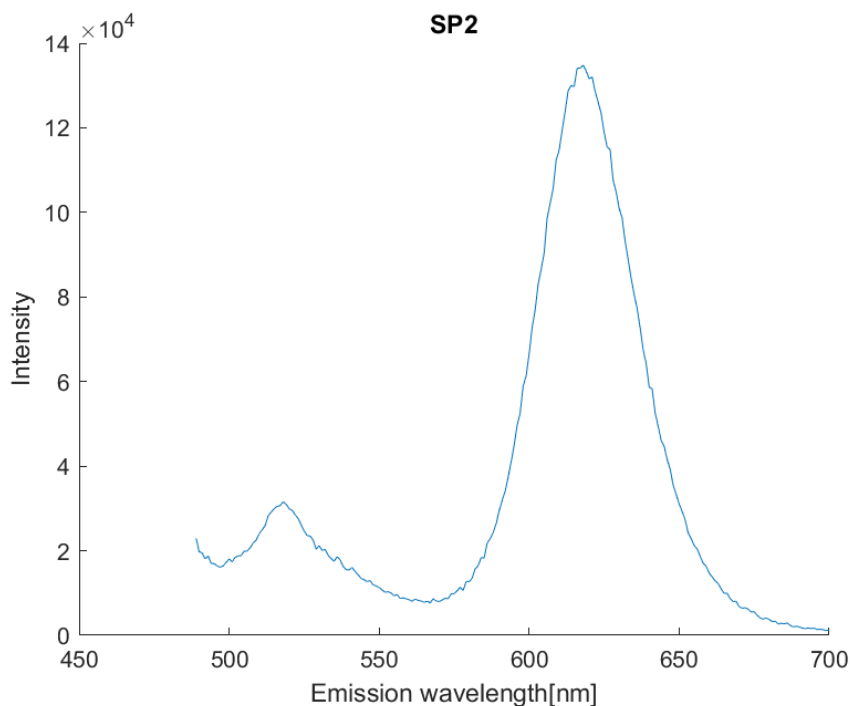


**Figure 7.20:** Fluorescence emission measurement of super nanoparticle synthesis products of SP2. Left peak wavelength is 518, right peak wavelength us 618. Excitation wavelength of 475nm.

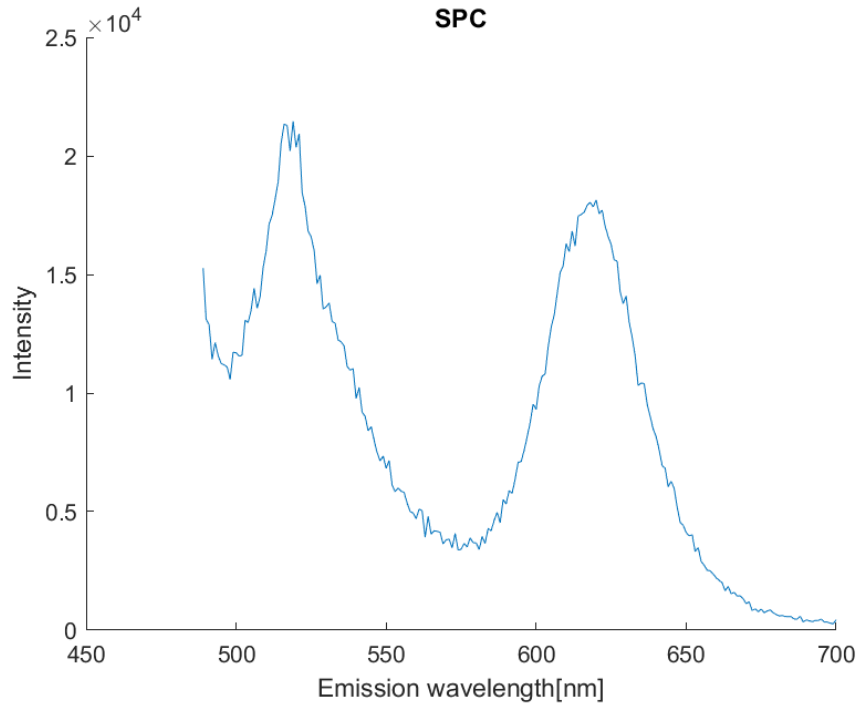


**Figure 7.21:** Fluorescence emission measurement of super nanoparticle synthesis products of SPC. Left peak wavelength is 519, right peak wavelength is 620. Excitation wavelength of 475nm.

The rightmost peak of these fluorescence measurements match the peak of quantum dots synthesized using method 2 with CdS shell.

## 7.6 Fluorescence Microscopy of Super Nanoparticles

To verify the magneto fluorescent properties of the synthesized supernanoparticles, particles were collected at the side of a microwell with an external magnet and imaged using fluorescence microscopy. Images for the samples SP1, SP2 and SPC can be seen in figure 7.22, figure 7.23 and figure 7.24 respectively.

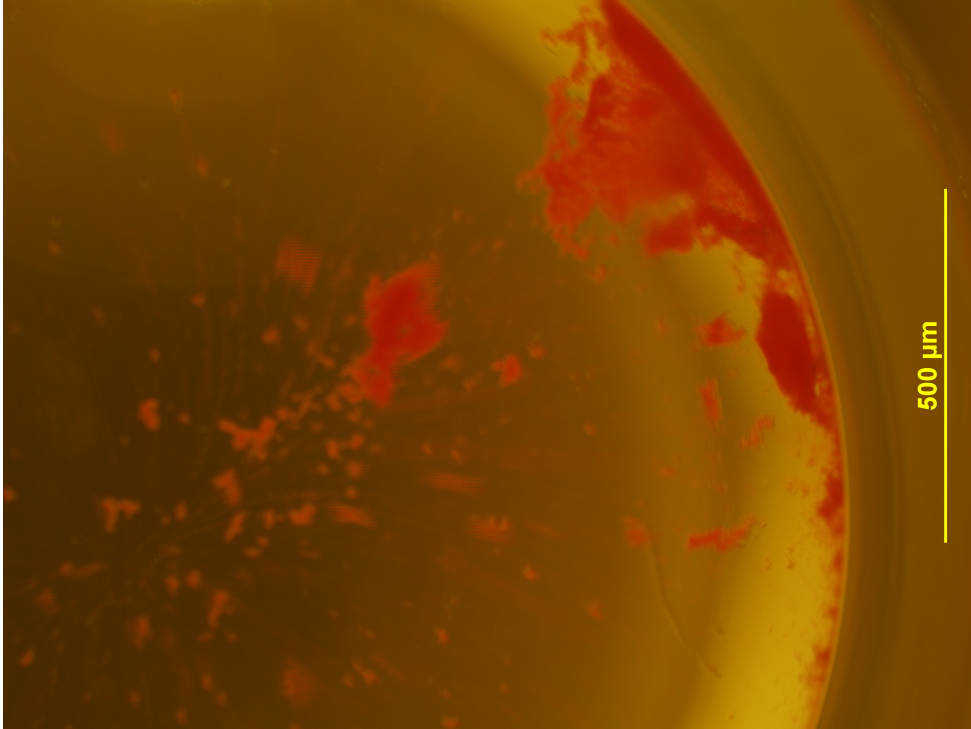


**Figure 7.22:** Fluorescence microscopy imaging of a microwell with SP1 particles gathered on the right side.

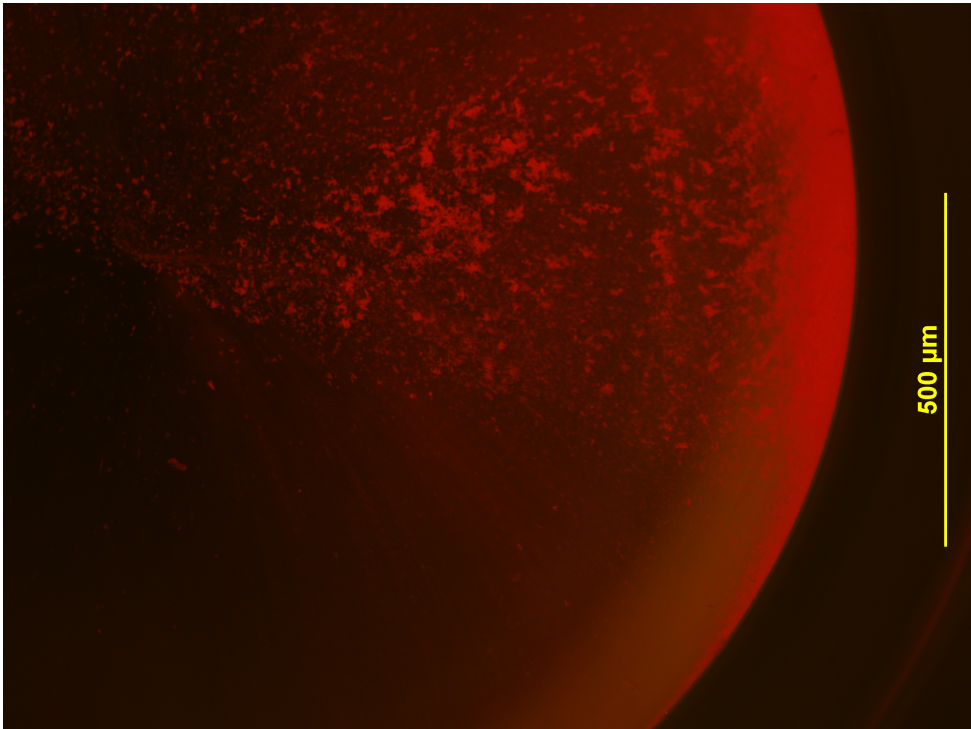


**Figure 7.23:** Fluorescence microscopy imaging of a microwell with SP2 particles gathered on the right side.

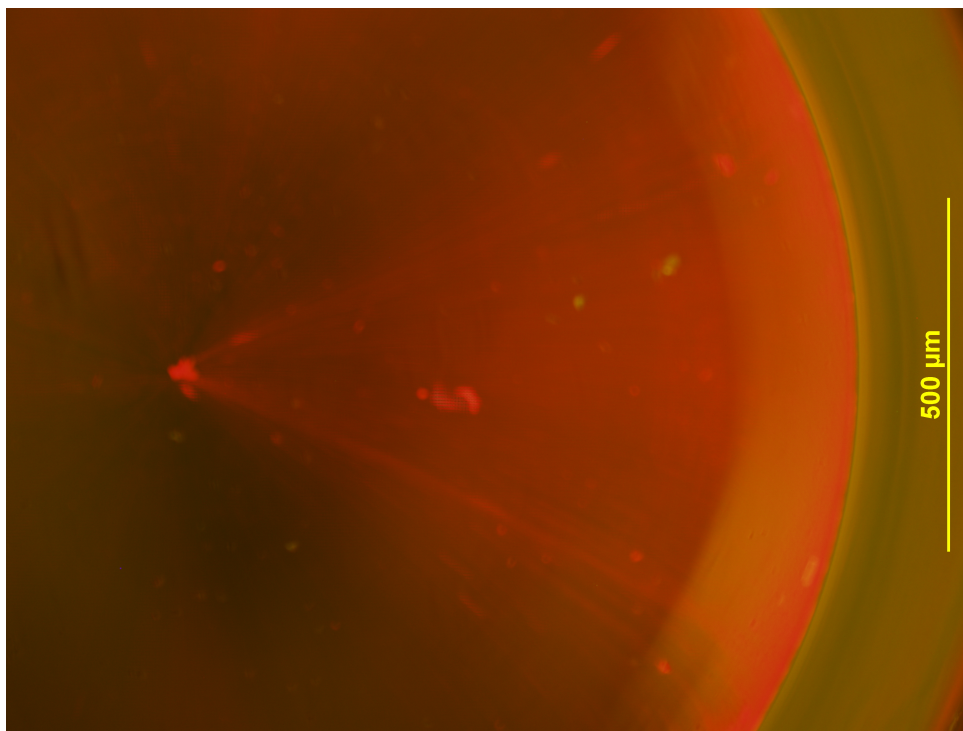


**Figure 7.24:** Fluorescence microscopy imaging of a microwell with SPC particles gathered on the right side.

The particles can be seen to be aggregated on the right side of the images. Not all particles in the well are gathered in this aggregate, with particles also found on the bottom of the well and moving in the solution (here seen as long streaks due to exposure times). Moving particles are particularly present in the SPC sample.

## 7.7 NTA measurements of Super Nanoparticles

Size characterization of the supernanoparticles was done using NTA. NTA measurements for SP1 and SP2 can be seen in figures 7.25 and 7.26 respectively. The measurements were significantly hindered by convection in the ethanol solution close to the laser thumbprint, significantly reducing the quality of measurements, and preventing acceptable measurements of SPC.

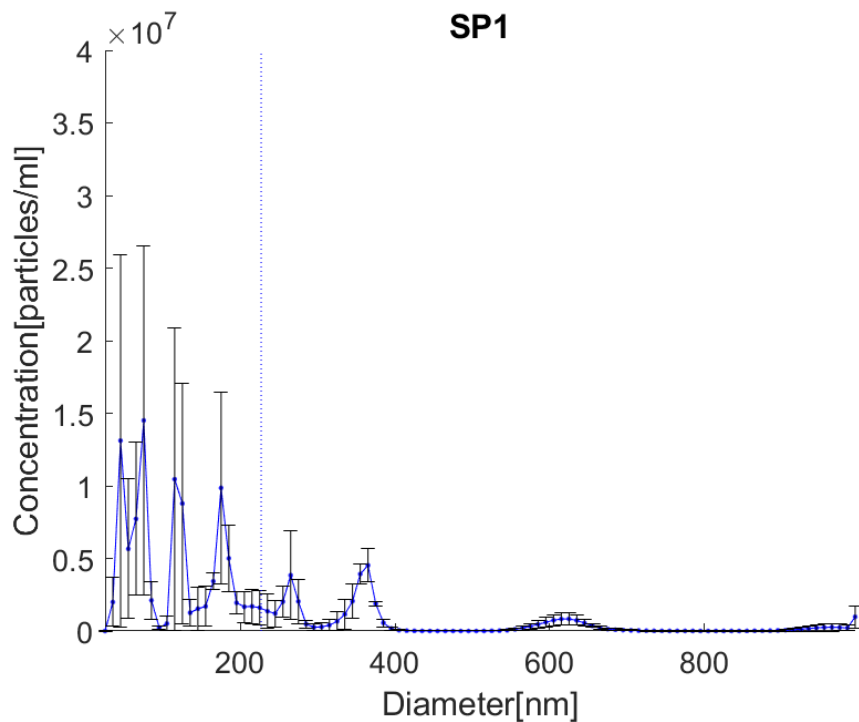


**Figure 7.25:** NTA measurements of SP1 supernanoparticles. The blue dotted line marks the mean size at 227nm with a standard error of 47nm.

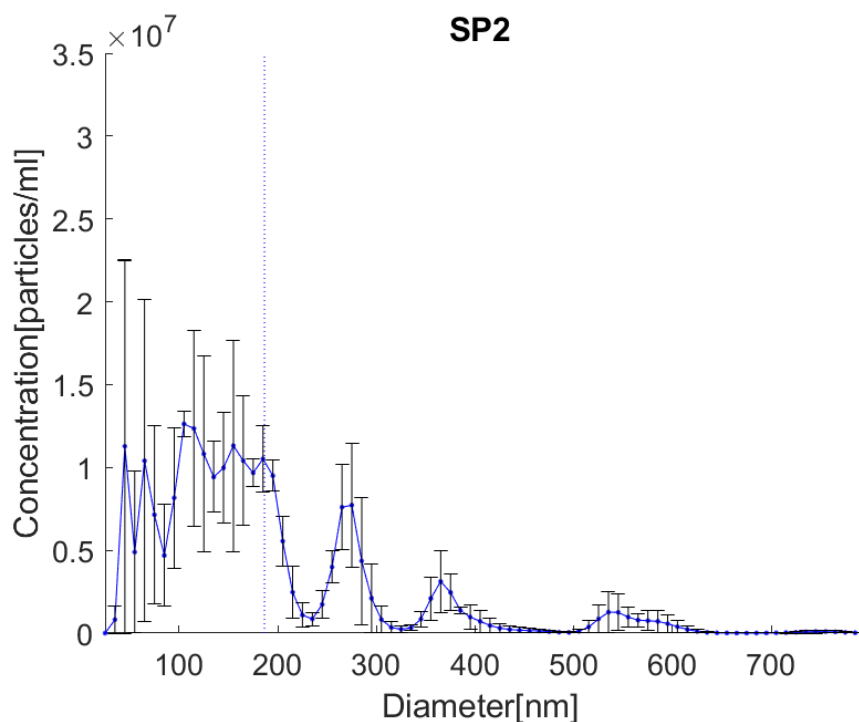


**Figure 7.26:** NTA measurements of SP2 supernanoparticles. The blue dotted line marks the mean size at 187nm with a standard error of 17nm.

The NTA measurements show significant errors, though particles for SP1 and SP2 gen-

erally fall in the range from below 100nm to 400nm with an additional peak at around 500-600nm. SP1 has a mean size of 227nm with a standard error of 47nm, while SP2 has a mean size of 187nm with a standard error of 17nm.

## 7.8 STEM Imaging and EDS Spectroscopy of Super Nanoparticles

STEM imaging was done to characterize the nanostructure of the supernanoparticles. STEM images of SP1 and SP2 can be seen in figure 7.27 and figure 7.28, respectively.

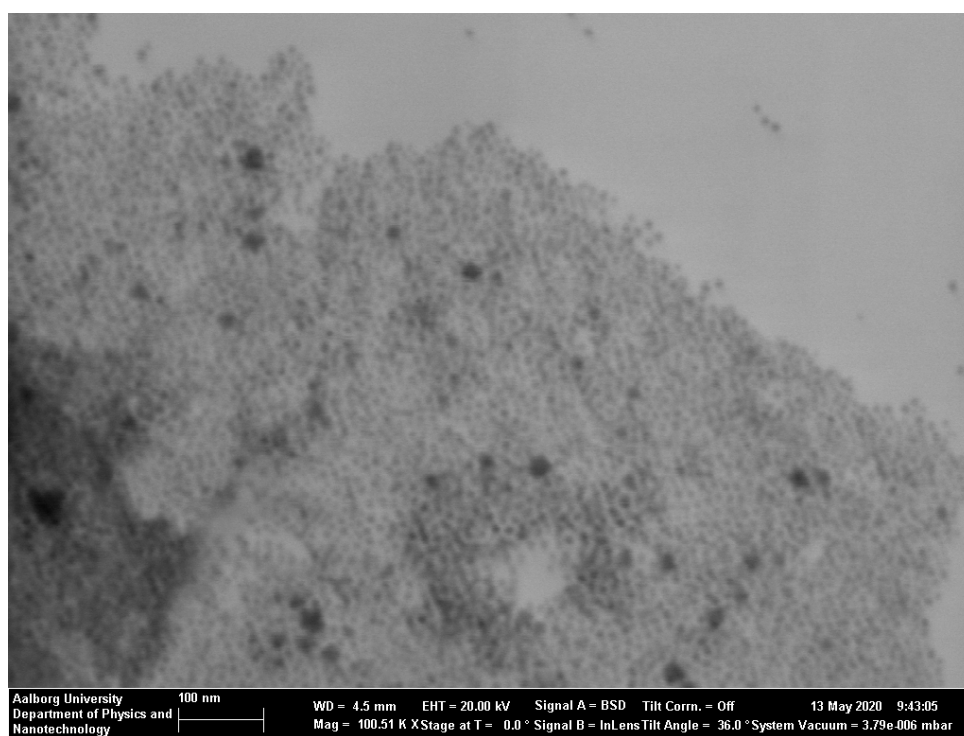


**Figure 7.27:** STEM image of SP1. The image show constituent nanoparticles without any superstructure.

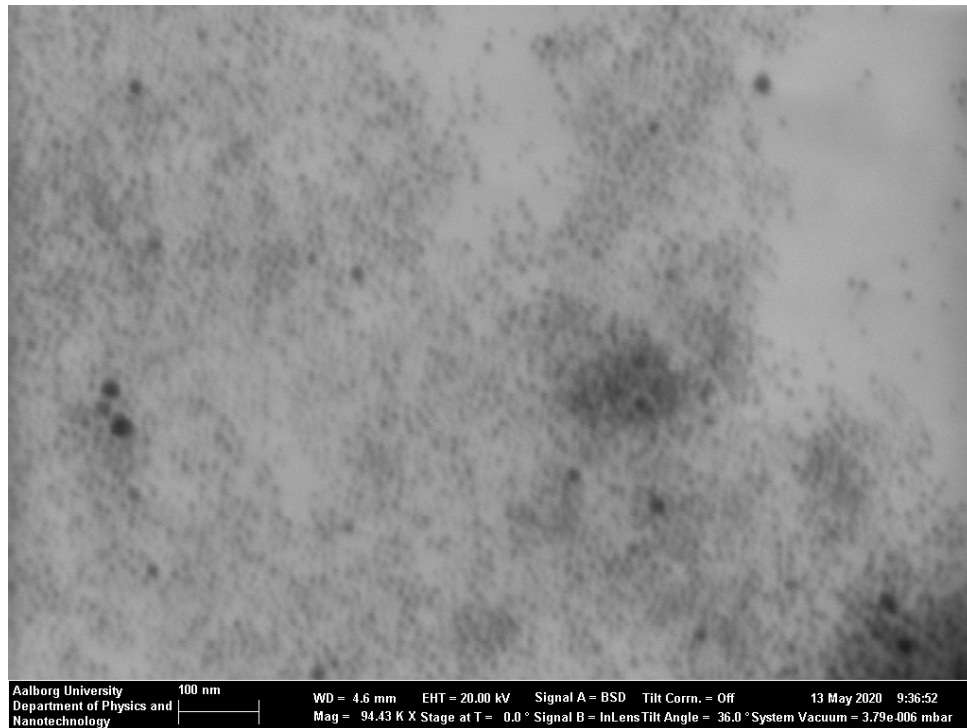


**Figure 7.28:** STEM image of SP2. The image show constituent nanoparticles without any superstructure.

The images for SP1 and SP2 show particles in the estimated size range of the constituent quantum dots and iron oxide nanoparticles, approximately 9nm to 15nm, though resolution is deemed insufficient for quantitative analysis. However, no superstructure can be observed. STEM images of SPC can be seen in figure 7.29 and figure 7.30.

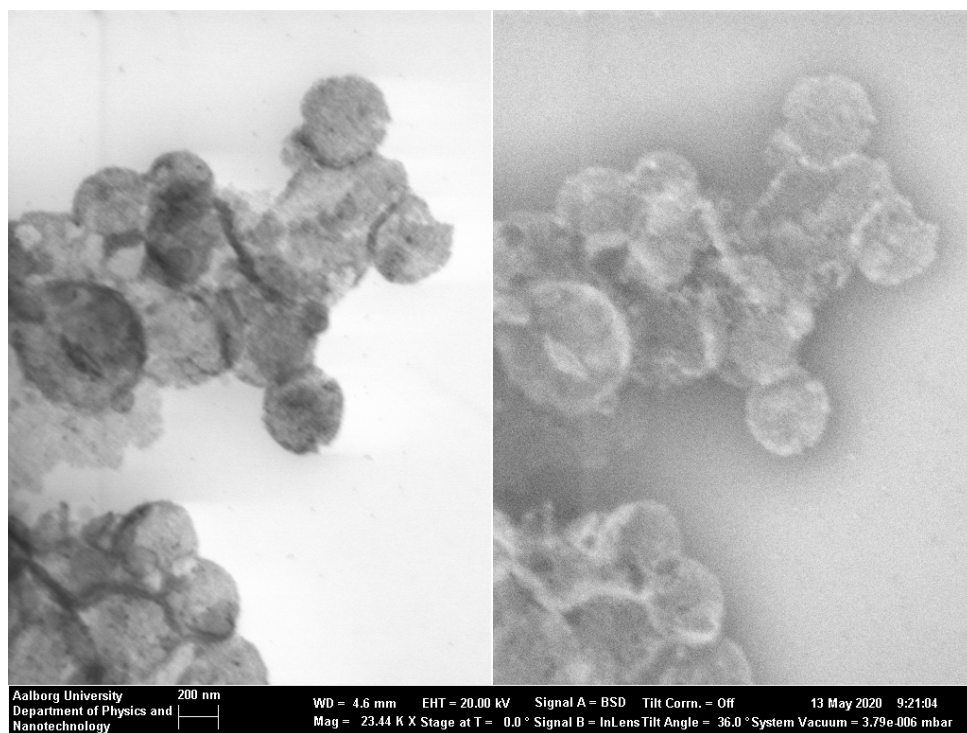


**Figure 7.29:** STEM image of SPC. The image show a defined circular or spherical superstructure, that is somewhat aggregated.

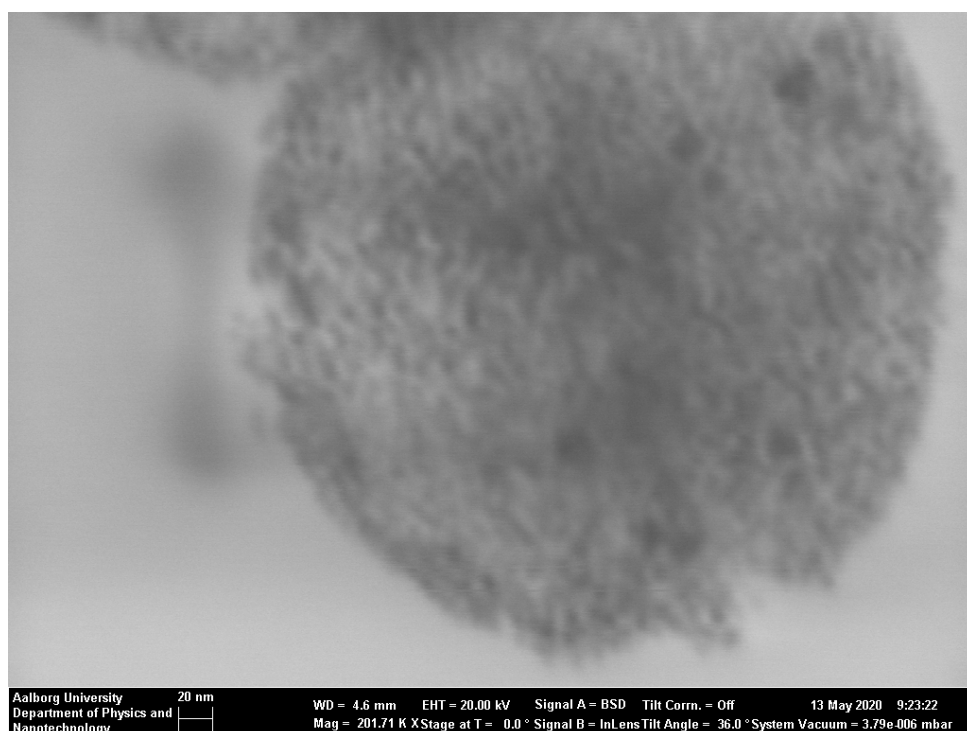


**Figure 7.30:** STEM image of SPC. The image show constituent nanoparticles within the circular superstructure.

Figure 7.29 clearly show circular superstructures, though with some aggregation of these.

These superstructures are in the size range between approximately 400nm to 600nm. On figure 7.30 the presence of the constituent nanoparticles can vaguely be resolved.

EDS measurements were performed to confirm the presence of iron oxide nanoparticles as well as CdSe quantum dots. In figure 7.31 EDS measurements of SP2 can be seen. For the measurements of the particles, both iron and cadmium can be detected compared to the background measurement where these elements are not present. Similarly, in figure 7.32, EDS measurements can be seen for the circular superstructures. Similar measurements are seen here, iron and cadmium can be detected at the superstructures while none can be detected from the background.

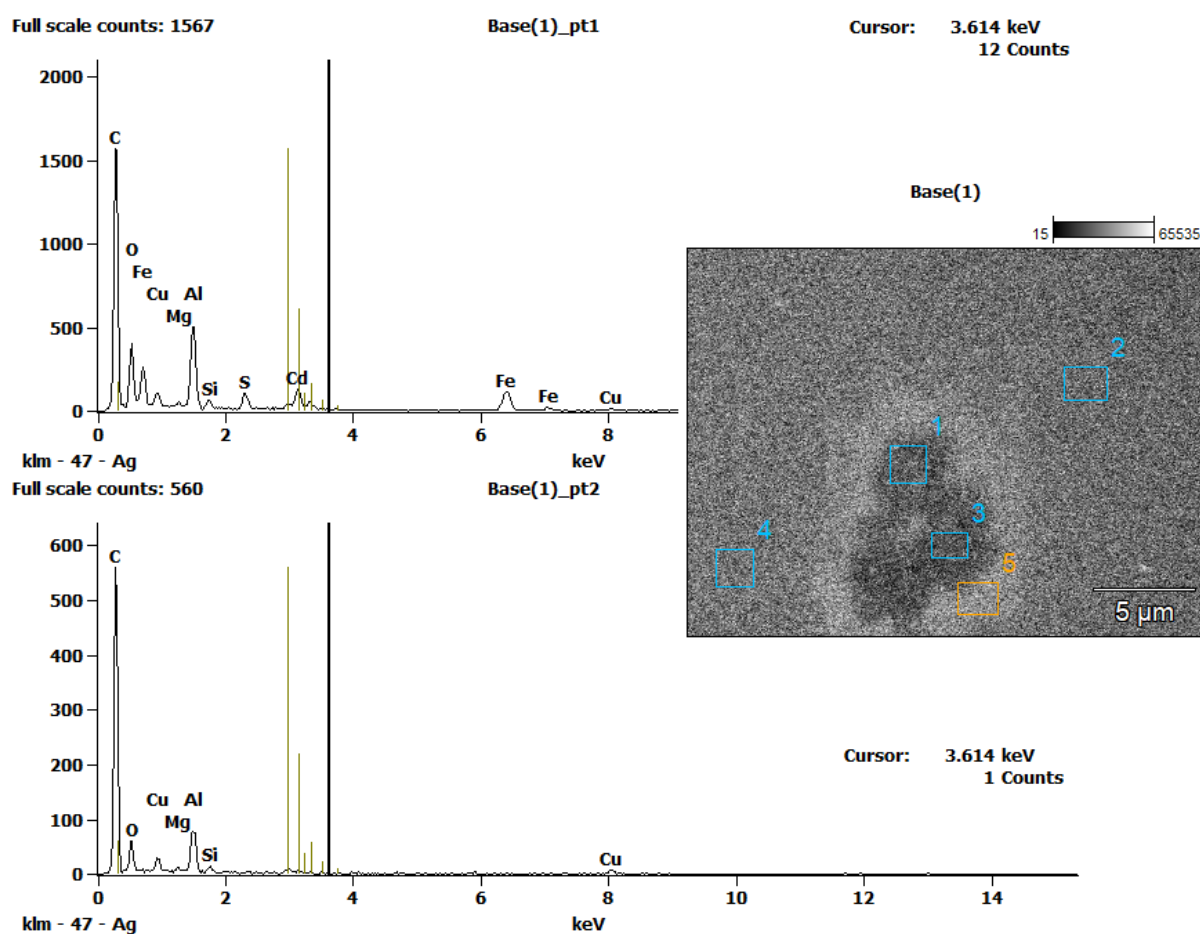


**Figure 7.31:** EDS measurements of SP2. Measurements show the presence of cadmium and iron on the particles, while none of these elements can be detected from the background.

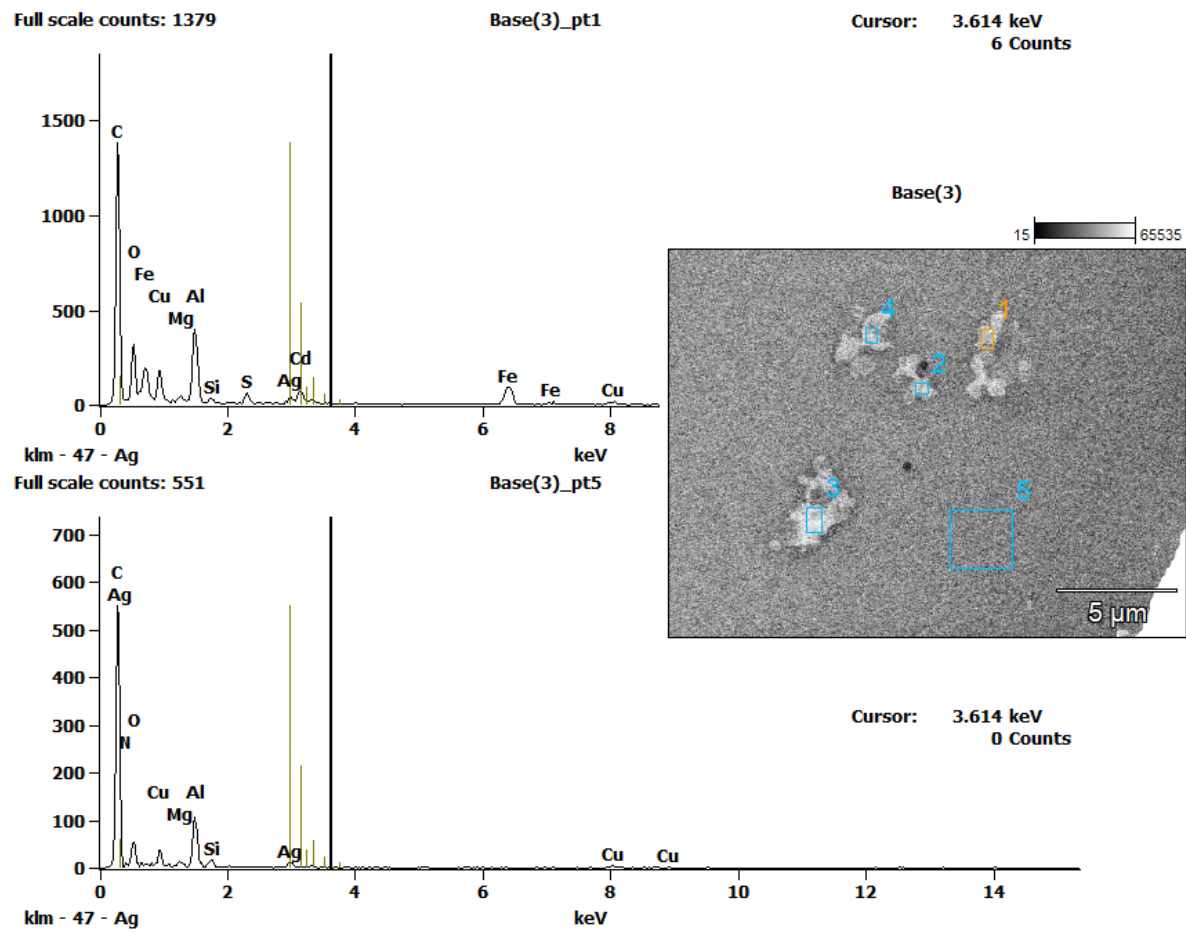


**Figure 7.32:** EDS measurements of SPC. Measurements show the presence of cadmium and iron on the superstructures, while none of these elements can be detected from the background.



---

## 8. Discussion

---

In the following chapter, the results of the project will be discussed. Firstly, the synthesis and characterization of the two methods of iron oxide nanoparticles will be discussed, Next, the results of the quantum dot synthesis, including CdS shell formation, will be discussed. Finally the results concerning the supernanoparticles will be discussed.

### 8.1 Iron Oxide Nanoparticles

Two methods of iron oxide nanoparticle synthesis was performed. Firstly the co-precipitation method of synthesis, along with silica shell coating, will be discussed, followed by discussion of the results of the thermal decomposition synthesis.

#### 8.1.1 Co-Precipitation Synthesis of Iron Oxide Nanoparticles

Iron oxide nanoparticles were synthesized using a modified co-precipitation method. This co-precipitation used a ratio of ferrous to ferric iron ion of 2, compared to a stoichiometric ratio for magnetite at 0.5, and used dropwise addition of the alkaline solution. This was done to improve iron oxide nanoparticle crystallinity and increase particle size.[11] Synthesis of iron oxide nanoparticles using this method have shown a median size of 24.6nm in literature.[11] NTA measurements of the synthesized particles showed a mean size of 81.2nm with a standard error of 17.7nm, see figure 7.1. This size is significantly larger, though includes the hydrodynamic radius when measured using NTA. SEM images of the same particles, see figure 7.3, show much smaller particles with diameters in the range of 25nm to 50nm. However the presence of small aggregates of multiple particles are present on the sample, see figure 7.4. It is unknown If this aggregation is present in the dispersion, though the NTA measurements show particles in a size range much larger than the individual particles which can be explained by the presence of larger aggregates.

#### 8.1.2 Silica Coating of Iron Oxide Nanoparticles

NTA measurements of the silica coated particles show much larger mean sizes, at 188.7nm with a standard error of 24.4nm, see figure 7.2. However, it can be observed from the SEM images of the same particles, see figure 7.7, that no meaningful change in the individual particle size is shown, certainly not on the scale observed with NTA. However in the

same SEM images, significantly larger aggregates can be seen, with no individual particles present. The same aggregation can be observed on the images before silica coating, with oleic acid stabilization, see figure 7.5. As such this aggregation cannot be attributed to the coating process. It is still unknown if this aggregation is caused by some step in the sample preparation or during sample deposition for the SEM measurement, and the increase in the NTA measurements are caused by some other factor.

### 8.1.3 Thermal Decomposition Synthesis of Iron Oxide Nanoparticles

Iron oxide nanoparticles synthesized through the thermal decomposition method were characterized using DLS. The expected size of the particles based on the synthesis is 5.9nm with a standard error of 0.3nm.[3] The intensity distribution showed the presence of a broader range of particles, from 10nm to 200nm with a small peak at 5000nm, see figure 7.9. The number distribution of the same measurement show major sharp peaks at 4.2nm, 15.7nm and 2.0nm, 7.10. It must be noted that the intensity distribution is more reliable and shows the presence of larger particles not seen on the number distribution. However, the number distribution show a overwhelming presence of smaller particles, though with significant uncertainty in the actual sizes. As such the size range of most of the smaller iron oxide nanoparticles can only be estimated to a range of approximately 2nm to 30nm.

## 8.2 Quantum Dots

The results of synthesis, based on absorbance spectroscopy and fluorescence spectroscopy, of quantum dots using method 1 and 2 will be discussed in the following sections. Additionally CdS shell formation will be discussed.

### 8.2.1 Method 1

The results of the reaction time on quantum dot synthesis using method 1 was presented in figure 7.11 and figure 7.13. The absorbance spectrum for the different reaction times show, as mentioned previously, a clear movement of the first absorption peak to higher wavelengths and increased absorption. This correspond well with growth of the particles from free monomers, changing the optical properties of the quantum dots by reducing the band gap. Increased absorption is also easily attributed to the increased size. At the 10min mark, particle development with time drastically changes. Growth at this stage is likely affected by the gradual loss of free monomers, which would lead to increased poly-

dispersity and eventual Ostwald ripening. However, as no size increase is observed after 10 minutes, Ostwald ripening seems less likely. The loss of absorbance characteristics with longer reaction time might then be attributed to increased polydispersity or aggregation of particles during the synthesis.

### 8.2.2 Method 2

Absorbance measurements of quantum dots synthesized using method 2 shows similar loss of absorbance characteristics, though much earlier, with increasing reaction time, though has little size development before this, see figure 7.12 and figure 7.14. The almost immediate development of the particles followed by quick degradation is likely attributed to the much higher concentration of reactants along with higher reaction temperature. Faster nucleation would result in faster depletion of free monomers. The higher temperature might also be responsible for faster aggregation of nanoparticles. The synthesis generally seems more sensitive to initial experimental conditions rather than reaction time. This is reflected in the differing results gained from stock synthesis.

The size dependence on experimental conditions is described in section 7.4, and is further elucidated using fluorescence spectroscopy. The WHHM of the fluorescence emission peak can here be used as an estimate of particle polydispersity.[10]

Significant reduction in particle size was obtained when the reaction mixture was left to rest after degassing. Without rest, particles with size of 613nm and 596nm were obtained, and showed the lowest polydispersity, based on the FWHM measurement. Completely monodisperse quantum dots have a FWHM measurement of approximately 20nm, which is close to the values obtained at 25nm and 26nm. With rest between degassing and synthesis, particles with sizes of 574nm and 545nm were obtained. Additionally a higher polydispersity was obtained, at 37nm FWHM measurement. With rest, the reaction mass is likely more exposed to oxygen after degassing, which is a likely cause of the size difference.

An attempt to reduce solvent loss during synthesis, by reducing nitrogen flow during synthesis resulted in significant reduction of absorbance characteristics, and a very large FWHM measurement of 60nm was obtained. Reduced nitrogen flow resulted in the reduced agitation of the reaction mass and increased oxygen during synthesis, both of which are likely causes for the deterioration of the particles.

The synthesis was also altered to double the solvent in the Se injection, to reduce concentration and nucleation speed, as well as improve the degassing procedure by flushing

with nitrogen. The resulting particles were smaller at 562nm, with a FWHM at 34nm.

### 8.2.3 CdS Shell Synthesis

After CdS shell formation a significant shift of the peak absorption wavelength was observed, see figures 7.15, 7.16, 7.17 and 7.18. The shift for particles synthesized using the first method was from 589nm to 630nm, and for particles synthesized using method 2, the wavelength shift was 563nm to 618nm. This shift is expected, and is the result of weak exciton confinement of the CdS shell.[14] FWHM measurements also increase after CdS shell synthesis, from 33nm to 52nm for synthesis method 1, and from 37nm to 42nm for synthesis method 2. Single quantum dot FWHM remains on the order of 20nm after addition of CdS shell,[14] and as such an increase in the FWHM measurement still indicates increased polydispersity. Consequently, a much higher increase in polydispersity is observed for synthesis method 1, despite a thicker shell synthesis for the second synthesis. A likely cause is the use of a drip funnel for the addition of reactants for synthesis method 1 particles, which was unreliable and produced higher flow rates than intended. Particles from both synthesis methods show an increase in polydispersity, though the synthesis is reported to maintain size distribution.[14]

## 8.3 Supernanoparticles

Supernanoparticle assembly failed multiple times. Only after thorough washing of both iron oxide nanoparticles and quantum dots was successful dispersion of the particles in ethanol achieved. A key step of the supernanoparticle assembly is the formation of dodecyltrimethylammonium bromide micelles. It is possible excess compounds from the synthesis of iron oxide nanoparticles or quantum dots interfered in the formation of micelles, or prevented the incorporation of the nanoparticles into the micelles. Supernanoparticle assembly using quantum dots, synthesized through method 2, without CdS shell also failed. The major difference between synthesis method 2 particles and the other quantum dots, is the lack of both octadecene for synthesis and oleic acid for stabilization. As such, it appears the resulting surface coating is incompatible with this supernanoparticle assembly. Quantum dots from synthesis method 1 produced particles that were able to be dispersed in ethanol, though these produced no detectable fluorescence emission, compared to particles with CdS shell from both synthesis methods that did show fluorescence. Quantum dot fluorescence is highly dependant on the surface of the crystal.[17] If the supernanoparticle assembly proved an environment unsuitable for quantum dot fluorescence, the increased isolation provided by the CdS shell might improve quantum dot fluorescence

under these conditions. Supernanoparticles also showed significantly reduced fluorescence compared to free quantum dots. As such, quantum dots without CdS shell, which showed darker fluorescence, might have been overshadowed by this reduction. Characterization was performed on three different samples, using washed iron oxide nanoparticles and CdS shell quantum dots synthesized through method 2 as the constituent nanoparticles, see section 7.5. The fluorescence spectra of SP1, SP2 and SPC are all similar, with two peaks, see figures ??, ?? and ?. The higher wavelength peak correlates to the emission peak of the constituent quantum dots, and has much higher intensity for SP2, due to the higher ratio of quantum dots. The lower wavelength peak was traced back to a likely contamination of the oleic acid used in the synthesis of the nanoparticles.

The magneto fluorescent properties of the assembled supernanoparticles are demonstrated in figures 7.22, 7.22 and 7.22. Of note is the fact that the majority of particles remain both magnetic and fluorescent after precipitation and resuspension. The particles remained mobile after being gathered to the side of the microwell, quickly redispersing in the solution after removal of the magnetic field. As such, it is difficult to conclude if the particles that are observed to be in dispersion are magneto-fluorescent or not. Of note is the fact that particles of SPC were significantly more mobile than the other samples.

For NTA, this mobility, likely due to convection created by the laser illumination, significantly hindered measurements. Measurements close to the laser thumbprint proved infeasible due to particle movement, requiring measurements to be taken far from the laser thumbprint for SP1 and SP2. This caused a greater amount of particles to be beyond the depth of field and poorer illumination. Additionally, the effects of the convection that remained for these measurements was unaccounted for. The SPC sample proved to have too high convection to make any measurement feasible. While an estimate of mean particle size was gained at 227nm and 187nm with a standard error of 47nm and 17nm for SP1 and SP2 respectively, see figure 7.25 and figure 7.26, these measurements are considered unreliable. The best estimate from these measurements is that particle size falls within a range below 600nm.

Much more reliable observations of the supernanoparticles were gained from STEM imaging, see figures 7.27, 7.28, 7.29 and 7.30. For samples SP1 and SP2, the constituent nanoparticles can be seen with no major superstructure, while for SPC, spherical, somewhat aggregated, superstructures can be seen. Little information is gained of the size of the superstructures in solution due to the likely deformation during sample preparation. Similarly, it is unknown if the aggregation of the spherical superstructures is present in the dispersion. The particles are confirmed as the constituent particles through the use

of EDS measurement, see figure 7.31 and figure 7.32. From these measurements, the presence of both iron and cadmium is confirmed within the observed nanoparticles, for both SP1 and SPC. The core-shell structure reported for the synthesis[3] is not directly observed, though this is possible due to the inability to directly distinguish the different nanoparticles.

The major difference between the two groups of supernanoparticles is the use of centrifugation for the precipitation of SPC. Firstly, it must be considered that both sample groups exhibit magneto fluorescent properties, and as such SP1 and SP2 likely have some superstructure before STEM sample preparation. Two likely factors causing the difference between the sample groups are magnetic selectivity when precipitating, and the difference in shear forces between magnetic precipitation and centrifugation. When precipitating the particles using an external magnet, only magnetic species are precipitated, along with anything bound to these magnetic species. As the particles are stabilized using PVP, this magnetic selectivity might cause a dilution of PVP after redispersion, as compared to precipitation using centrifugation, where a larger mass of PVP might be precipitated along with the particles. This might cause a weakening and/or deformation of the supernanoparticle structure that result in complete disassembly upon STEM sample preparation. The other likely factor is the difference in shear forces between magnetic precipitation and centrifugation. If the shear forces experienced by the particle during the much longer period of magnetic precipitation, is more damaging to the stability of the superstructure than those experienced during centrifugation, the supernanoparticle superstructure might be sufficiently damaged to similarly disassemble upon STEM sample preparation.

---

## 9. Conclusion

---

In conclusion, iron oxide nanoparticles and quantum dots with CdS shell were successfully synthesized, along with the assembly of a superstructure combining both particles.

Iron oxide nanoparticles were firstly synthesized using a co-precipitation method. The iron oxide nanoparticles showed mean sizes of 81.2nm with a standard error of 17.7nm. Silica coating was attempted for these particles to test the protocol, but successful coating was never confirmed. Iron oxide nanoparticles were also synthesized through a thermal decomposition method. A rough estimate put the size of the large population of smaller nanoparticles in a range between 2nm and 30nm. Quantum dots were synthesized through two methods, a lower temperature method, and a higher temperature method. A wide range of nanoparticles were synthesized using both methods, with stock dispersions made with sizes of 3.8nm and 2.9nm for the first and second method respectively. CdS shell synthesis was successfully performed for particles from both methods. Finally supernanoparticles were assembled using iron oxide nanoparticles synthesized through the thermal decomposition method and quantum dots synthesized through the high temperature method, with a CdS shell. The resulting particles showed clear magnetic and fluorescent properties, though the presence of a nanoparticle superstructure as observed with STEM imaging was highly dependent on the precipitation method during the assembly.



---

## 10. Further Experimentation

---

In the following chapter, further avenues for possible experimental work will be detailed.

Firstly, the quantum dots synthesized differed not only in regards to absorption and fluorescence, but also in regards to quantum yield, particularly between quantum dots with and without CdS shell. As no efforts were made to characterize the quantum yield, this was not discussed further. However efforts should be made to characterize quantum yield to effectively compare and evaluate the different synthesized quantum dots.

Supernanoparticle assembly was only briefly attempted. Proper examination and optimization of the assembly process should be done. Additionally supernanoparticles with differing sizes and ratios of iron oxide nanoparticles to quantum dots can be assembled to suit the requirements of the application.

Silica coating of the supernanoparticles would be the next step of preparation of the drug delivery vehicle. This would additionally likely allow for better characterization using STEM, as the stability of the supernanoparticle structure is strongly stabilized. With silica coating the possibility of surface functionalization becomes very feasible. Of particular interest is functionalization of the nanoparticle surface using transferrin, or a suitable antibody, allowing for exploration of this receptor pathway in combination with magnetic guidance. Exploration of this pathway of course requires a suitable model. In vitro blood brain barrier models are suitable for experimentation exploring the effects of nanoparticle size, surface functionalization and the magnitude of magnetic guidance across the barrier.



---

# Bibliography

---

- [1] Tatiana Barichello *et al.* “An Overview of the Blood-Brain Barrier”. In: *Neuromethods* 142 (2019), pp. 1–8.
- [2] Brian M. Kopec *et al.* “Methods of Delivering Molecules Through the Blood-Brain Barrier for Brain Diagnostics and Therapeutics”. In: *Neuromethods* 142 (2019), pp. 9–43.
- [3] Ou Chen *et al.* “Magneto-fluorescent core-shell supernanoparticles”. In: *Nat Commun* 5.5093 (2014).
- [4] Andreas M. Grabrucker *et al.* “Nanoparticles as Blood–Brain Barrier Permeable CNS Targeted Drug Delivery Systems”. In: *Top Med Chem* 10 (2014), pp. 71–90.
- [5] Anne Mahringer *et al.* “The Blood–Brain Barrier: An Introduction to Its Structure and Function”. In: *Top Med Chem* 10 (2014), pp. 1–20.
- [6] Maja Habulin *et al.* “Biocompatible Nanomaterial: Synthesis, Characterisation And Applications”. In: *Magnetic Nanoparticles: Properties, Synthesis and Applications* 1 (2012), pp. 135–156.
- [7] Xin Chu *et al.* “Overview of Synthesis of Magnetic Nanomaterials”. In: *Magnetic Nanomaterials: Fundamentals, Synthesis and Applications* 1 (2017), pp. 83–120.
- [8] Vladimir L. Kolesnichenko. “Synthesis of Nanoparticulate Magnetic Materials”. In: *Magnetic Nanoparticles* 1 (2009), pp. 25–58.
- [9] Stefan Kudera *et al.* “Growth mechanism, shape and composition control of semiconductor nanocrystals”. In: *Semiconductor Nanocrystal Quantum Dots: Synthesis, Assembly, Spectroscopy and Applications* 1 (2008), pp. 1–34.
- [10] Peter Reiss. “Synthesis of semiconductor nanocrystals in organic solvents”. In: *Semiconductor Nanocrystal Quantum Dots: Synthesis, Assembly, Spectroscopy and Applications* 1 (2008), pp. 35–72.
- [11] T *et al.* Iwasaki. “Size control of magnetite nanoparticles by organic solvent-free chemical coprecipitation at room temperature”. In: *Journal of Experimental Nanoscience* 5 (2010), pp. 251–262.
- [12] JONGNAM PARK *et al.* “Ultra-large-scale syntheses of monodisperse nanocrystals”. In: *nature materials* 3 (2004), pp. 891–895.

- 
- [13] *Synthesis of Cadmium Selenide Quantum Dot Nanoparticles*. <https://education.mrsec.wisc.edu/preparation-of-cdse-quantum-dot-nanoparticles/>. Accessed: 2020-01-13.
- [14] Ou Chen *et al.*. “Compact high-quality CdSe–CdS core–shell nanocrystals with narrow emission linewidths and suppressed blinking”. In: *Nat Commun* 12 (2013), pp. 445–451.
- [15] Haitao Liu *et al.*. “Solution structure of cadmium carboxylate and its implications for the synthesis of cadmium chalcogenide nanocrystals”. In: *Chem. Commun* 49 (2013), pp. 7857–7859.
- [16] W. William Yu *et al.*. “Experimental Determination of the Extinction Coefficient of CdTe, CdSe, and CdS Nanocrystals”. In: *Chemistry of Materials* 15.14 (2003), pp. 2854–2860.
- [17] J. Jack Li *et al.*. “Large-Scale Synthesis of Nearly Monodisperse CdSe/CdS Core/Shell Nanocrystals Using Air-Stable Reagents via Successive Ion Layer Adsorption and Reaction”. In: *J. AM. CHEM. SOC* 125 (2003), pp. 12567–12575.